The Astrophysical Journal, 987:192 (16pp), 2025 July 10 https://doi.org/10.3847/1538-4357/addbe3

A Numerical Model for the Dynamics of Pickup Ions Outside the Heliopause and IBEX "Ribbon" Observation

Yifan Huang[1], Fan Guo[1], Eric J. Zirnstein[2], Sung Jun Noh[1], Hui Li[1], Daniel B. Reisenfeld[1], and Jacob Heerikhuisen[3]
[1] Los Alamos National Laboratory, Los Alamos, NM 87545, USA; huangyifan06005@gmail.com
[2] Princeton University, Princeton, NJ 08544, USA
[3] University of Waikato, Hillcrest, Hamilton 3216, New Zealand
Received 2024 December 19; revised 2025 May 17; accepted 2025 May 20; published 2025 July 8

Abstract

The leading mechanism for the origin of the Interstellar Boundary Explorer (IBEX) "ribbon" of enhanced energetic neutral atoms (ENAs) from the outer heliosphere is the so-called secondary ENA process. In this mechanism, neutralized ions escape the heliosphere, and after several times of charge exchange collision,s some propagate back toward Earth in directions nearly perpendicular to the local interstellar magnetic field. However, the physical processes governing the distribution of the pickup ions (PUIs) outside the heliopause are still unclear. In this study, we build a new global model of the IBEX ribbon, where a key component is to calculate the dynamics of the PUIs outside the heliopause by solving the gyrophase-averaged focused transport equations on top of the background magnetohydrodynamic-kinetic model for the heliosphere-interstellar medium interaction. We discuss how the properties of the simulated ribbon change with different scattering parameters and show simulation results of the ENA sky maps, ribbon centers, ribbon profiles at several azimuthal slices, the ribbon ENA source region, and the velocity distribution of PUIs in the ENA source region for different scattering frequencies. Our results show that the model can provide reasonable ribbon sky maps comparable to the observed ribbon when the PUI mean free path is on the order of several thousand astronomical units.

Unified Astronomy Thesaurus concepts: Pickup ions (1239); Heliosphere (711); Solar wind (1534); Charge exchange ionization (2056); Interstellar medium (847); Solar energetic particles (1491); Space plasmas (1544); Interstellar magnetic fields (845); Particle physics (2088)

1. Introduction

NASA's Interstellar Boundary Explorer (IBEX; D. J. McComas et al. 2009a) has been measuring energetic neutral atoms (ENAs) from the outer heliosphere and local interstellar medium (LISM) with energies ~300 eV to ~6 keV via the IBEX-Hi instrument (H. O. Funsten et al. 2009a) since 2008. IBEX-Hi revealed a feature of enhanced ENA intensity that stretches across much of the sky. This feature was unexpected before the mission and is now commonly referred to as the IBEX ribbon. The ribbon has an intensity ~2–3 times brighter than the surrounding globally distributed flux, and varies in width with a full width at half-maximum (FWHM) ranging from ~15° to ~25°, depending on the ENA energy channel (H. O. Funsten et al. 2009b; S. A. Fuselier et al. 2009; D. J. McComas et al. 2009b, 2010; S. J. Noh et al. 2025). The nearly circular arc is centered near the radial vector pointing toward (longitude, latitude) $(\lambda, \beta) = (221°, 39°)$ in the ecliptic J2000 coordinates (H. O. Funsten et al. 2009a). Comparing the ribbon observations with the three-dimensional models of the heliosphere, the ribbon ENA emission corresponds to the directions where the observer's line of sight (LOS) is approximately perpendicular to the interstellar magnetic field (ISMF), i.e., $\boldsymbol{B} \bullet \boldsymbol{r} \sim 0$ (N. V. Pogorelov et al. 2009; N. A. Schwadron et al. 2009).

To explain the origin of the IBEX ribbon, numerous theories and models have been developed (see D. J. McComas et al. 2014 and references therein, and also more recent models by P. A. Isenberg 2014; J. Giacalone & J. R. Jokipii 2015, and E. J. Zirnstein et al. 2020). Currently, the most accepted explanation for the ribbon is the "secondary ENA" mechanism, sketched in Figure 1. As the neutral interstellar wind flows inside the termination shock (TS) from the LISM, the supersonic solar wind (SW) flows outward from the Sun, moving at ~400 km s^{-1} near the equator and ~400–800 km s^{-1} near the poles depending on the time in the solar cycle, and some ions in the SW may charge exchange with interstellar atoms. These SW ions become primary ENAs that have the velocity and energy of the parent SW ions, and then move radially outward in the direction the SW is moving, forming the so-called neutral solar wind (NSW). With a charge-exchange mean free path (on the order of 1000 au) much larger than the heliosphere scale, these ENAs easily traverse the heliosphere and cross the heliopause into the denser LISM, shown as the red lines in Figure 1. Meanwhile, interstellar atoms that lose electrons to the NSW are picked up by the electromagnetic field of the outward-propagating SW and are referred to as interstellar pickup protons. They may undergo another charge exchange with interstellar atoms inside the TS to become interstellar neutrals that can also exit the heliosphere into the LISM, shown as the pink lines in Figure 1. In addition to the two sources of the primary ENAs mentioned above, hot ions in the inner heliosheath (IHS) may become heliosheath neutrals due to charge exchanges with interstellar atoms and then move into the LISM, shown as blue lines in Figure 1. These primary ENAs eventually become pickup ions (PUIs) through charge exchange

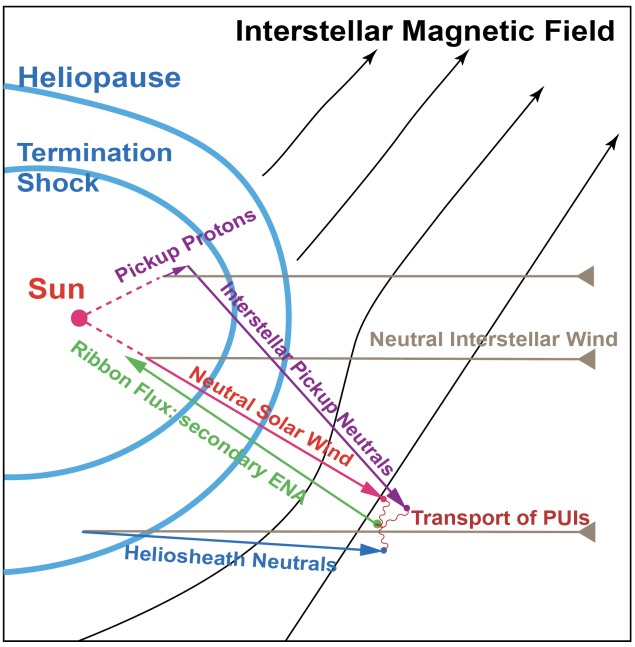

Figure 1. Schematic of the secondary ENA mechanism. The ribbon ENAs detected by IBEX (green vector) are coming from the charge exchange of PUIs beyond the heliopause. We show three primary ENA components that contribute to these PUIs: the NSW (red vector), the interstellar pickup neutrals (purple vectors), and the heliosheath neutrals (blue vector).

with the denser and cooler plasma in the LISM and gyrate about the ISMF lines, populating the suprathermal plasma of the LISM. During their mean lifetime of a couple of years, the PUIs can evolve in their distribution and propagate elsewhere, shown as the dark red curves in Figure 1. After undergoing one more charge exchange with neutrals in the LISM, the PUIs are converted to secondary ENAs, some of which may travel back to Earth depending on their locations and trajectories, and can be observed by IBEX.

The NSW source of PUIs for the ribbon, included in previous secondary ENA models (e.g., S. V. Chalov et al. 2010; J. Heerikhuisen et al. 2010; E. Möbius et al. 2013; N. A. Schwadron & D. J. McComas 2013; E. J. Zirnstein et al. 2013, 2016b, 2023; K. V. Gamayunov et al. 2017, 2019), has been found to dominate the emission of the ribbon ENA at energies less than 2 keV. The PUI source of interstellar pickup neutrals has been included in recent work (N. A. Schwadron & D. J. McComas 2019; E. J. Zirnstein et al. 2023), suggesting that interstellar pickup atoms in the SW dominate the ribbon signal in the ∼2–6 keV range, which corresponds to the IBEX-Hi Electrostatic Energy Analyzer (ESA) 4–6 energy passbands. Several studies (e.g., J. Heerikhuisen et al. 2010; E. J. Zirnstein et al. 2013, 2016a) have included the PUI source from the IHS neutrals and suggest that the IHS neutrals do not contribute significantly to the ribbon ENA fluxes measured below ∼6 keV.

In general, secondary ENA models are divided into two extreme scenarios, and each of these emphasizes different dynamic behaviors of the PUIs before becoming secondary ENAs. The first is the weakly scattering (or velocity retention) scenario, which suggests that PUIs gyrating about the ISMF could maintain an anisotropic ring-beam distribution before being neutralized (e.g., S. V. Chalov et al. 2010; K. Gamayunov et al. 2010; J. Heerikhuisen et al. 2010, 2014; E. Möbius et al. 2013; E. J. Zirnstein et al. 2013, 2015; K. V. Gamayunov et al. 2017). This scenario can successfully reproduce the ribbon in the direction $\boldsymbol{B}\cdot\boldsymbol{r}\sim 0$ because newly born PUIs are mostly gyrating perpendicular to the ISMF. One challenge to the weakly scattering model is that the ring-beam distribution is known to be unstable to the ion–cyclotron instability. This excites a broad spectrum of waves that subsequently scatter and isotropize the PUIs in a timescale (several days) much shorter than their lifetime (e.g., V. Florinski et al. 2010). It is worth noting that the stability of the ring-beam distribution of PUIs in the LISM is still in debate. For example, V. Florinski et al. (2016) show the presence of a "stability gap" in which the rings of injected protons could be retained for years in the presence of a warm Maxwellian core of plasma (see also E. J. Summerlin et al. 2014). In contrast, the latest work by K. Min & K. Liu (2018) and A. Mousavi et al. (2020, 2022) indicates that the stability of ring-beam distribution is not guaranteed once the mirror and the ion Bernstein instabilities are taken into account. Other than the microinstabilities of the ring-beam distribution, the pitch-angle scattering behavior of PUIs also depends on the degree of local interstellar turbulence (L. F. Burlaga et al. 2018). Simulations of K. Gamayunov et al. (2010) and K. V. Gamayunov et al. (2017, 2019) that include large-scale interstellar turbulence and small-scale instabilities support the stability of the anisotropy of PUIs. As detailed above, the kinetic physics associated with the stability of the PUI ring-beam distribution remains unclear. Although the weakly scattering model requires stability of the ring-beam distribution, it is likely that PUIs undergo some level of scattering but still maintain anisotropy in velocity space (J. Heerikhuisen et al. 2014; E. J. Zirnstein et al. 2019).

The spatial retention model, which was first introduced by N. A. Schwadron & D. J. McComas (2013), explains the ribbon as the result of a localized source region of the ribbon (where $\boldsymbol{B}\bullet\boldsymbol{r}\sim 0$) of inhibited spatial transport and (therefore) enhanced intensity of PUIs. N. A. Schwadron & D. J. McComas (2013) suggests that pickup protons, with initial streaming speeds less than the Alfvén speed ($u_{\parallel} < V_{\rm A}$), can be trapped near the $\boldsymbol{B}\bullet\boldsymbol{r}\sim 0$ plane by resonating with Alfvén waves propagating in the opposite direction to the proton motion along the magnetic field, resulting in a concentration of pickup protons at those locations. After that, many works (e.g., P. A. Isenberg 2014, 2015; J. Giacalone & J. R. Jokipii 2015; E. J. Zirnstein et al. 2019; S. Xu & H. Li 2023) have studied the mechanisms that can lead to spatial retention effects. For example, the works by P. A. Isenberg (2014, 2015) also have a similar picture but present a "dominant turbulence" approximation that considers self-generated turbulence instead of only Alfvén waves, resulting in much lower ENA fluxes. J. Giacalone & J. R. Jokipii (2015, 2020) suggest that the pre-existing turbulence in the LISM can efficiently trap ions with initial pitch angles near 90° by magnetic mirroring (see also E. J. Zirnstein et al. 2020; S. Xu & H. Li 2023). Compared with the weakly scattering model, the PUI velocity distribution in the ribbon source region is not ring-beam-like anymore and may vary due to different PUI trapping mechanisms. For example, in the work of N. A. Schwadron & D. J. McComas (2013) and P. A. Isenberg (2015) the distribution could be a nearly isotropic "bispherical" shape due to strong scattering in the source region of the ribbon, and in J. Giacalone & J. R. Jokipii (2015) the distribution may have an enhanced intensity of the "partial shell" around 90° due to mirroring. The ribbon simulation by E. J. Zirnstein et al. (2019), based on the spatial retention model in N. A. Schwadron &

D. J. McComas (2013), shows that the intensity of the ribbon is approximately two times less than that of the observation, indicating that an additional source of enhanced PUIs is needed. In addition, E. J. Zirnstein et al. (2020) study the effects of turbulence mirroring by simulating the ribbon in the presence of interstellar turbulence with different correlation lengths of the turbulence. They find that the large-scale structure of the ribbon is robust when the correlation length is $\lesssim$100 au.

In this work, we build a numerical ribbon model based on the secondary ENA mechanism to study the dynamics of PUIs beyond the heliopause and the resulting synthetic ENA sky maps. Our model does not have a specified scenario, i.e., weakly scattering or spatial retention, due to the debates among the aforementioned studies, but can be treated as a framework that includes a comprehensive set of energetic particle transport processes. We set up a realistic background plasma/neutral population and magnetic field within the heliosphere and LISM, using the global magnetohydrodynamic (MHD) simulation in E. J. Zirnstein et al. (2021b). The PUIs outside the heliopause are initialized according to the distribution functions of the primary ENAs in the LISM, which are calculated from averaged SW observation profiles (P. Swaczyna et al. 2016; E. J. Zirnstein et al. 2019). In our current stage, we do not include the PUIs coming from the interstellar pickup neutrals or the heliosheath neutrals, but only consider the PUIs from the NSW (PINS). Our model simulates the PUI dynamics by solving the gyrophase-averaged focused transport equations of PUI particles. The method is similar to that in K. V. Gamayunov et al. (2019), but we extend the region to the full three-dimensional simulation domain. In this work, we study the effects of PUI scattering/dynamics on the ribbon production by varying the pitch-angle diffusion coefficient over a wide range. We estimate the mean free path of PUIs outside the heliopause in order to produce ENA sky maps comparable with observations, which show that our model has the potential to test different secondary ENA scenarios.

This paper is organized as follows. In Section 2, we introduce the methodology of our ribbon model, including details of setting up the system environment (e.g., plasma/neutral properties and ISMF), simulating the dynamics of the PUI particles, and calculating the ENA flux intensity. In Section 3, we provide results of the simulated ribbon that can be compared with observations and study the effects of PUI pitch-angle scattering. Section 4 summarizes our main results and conclusions.

2. Methodology

The flowchart in Figure 2 summarizes the procedures in our numerical ribbon model. The model uses inputs, such as neutralized SW and local plasma/neutral properties beyond the heliopause, from a global heliosphere model and a neutral SW source model, detailed in Sections 2.1 and 2.2. Our work focuses mainly on computing the transport of PUIs by solving the gyrophase-averaged focused transport equation (Section 2.3). In this paper, we calculate the pitch-angle diffusion coefficient according to quasi-linear theory in cases with different mean free paths (see details in Section 2.3.2). By tracking the dynamics of PUIs and accumulating the neutralized SENAs, we compute the SENA flux observed by IBEX and produce synthetic ribbon sky maps (Section 2.4).

2.1. Simulation of the Heliosphere and the Local Interstellar Medium

We utilize plasma and neutral results from a three-dimensional MHD-plasma and kinetic-neutral simulation of SW–LISM interaction, similar to the work by E. J. Zirnstein et al. (2016b, 2019, 2020, 2021b). The simulation solves MHD equations for the SW and Boltzmann's equation for neutral hydrogen atoms, which are coupled by energy-dependent, charge exchange, and photoionization source terms (for more details, see N. V. Pogorelov et al. 2008; J. Heerikhuisen et al. 2010, 2015).

The LISM outer boundary conditions, imposed at 1000 au from the Sun, are primarily derived from IBEX-Lo and IBEX-Hi observations. The values used in the simulation are ISMF strength of 2.93 μG and direction (227.°28, 34.°62) in the ecliptic J2000 (E. J. Zirnstein et al. 2016b, 2021b), with which the simulation of the heliosphere produces a draped magnetic field that is consistent with the measurements of field magnitude and orientation by Voyager 1 at its location (E. J. Zirnstein et al. 2016b; A. Czechowski & J. Grygorczuk 2017). A recent comparison by J. S. Rankin et al. (2023) shows that the transverse components of the ISMF predicted in E. J. Zirnstein et al. (2016b) agree very well with the observations of the Voyagers, but the radial components have a clear discrepancy. Their findings raise the possibility that the magnitude and direction of the ISMF may differ from those derived independently from the IBEX ribbon (E. J. Zirnstein et al. 2016b). In our work, we treat the ISMF results from E. J. Zirnstein et al. (2016b) as still applicable because (1) uncertainties in the calibration methods of the Voyagers' radial magnetic field outside the heliosphere might render unreliable measurements (D. B. Berdichevsky 2009; J. S. Rankin et al. 2023), and (2) the transverse magnetic field components near the ENA source region dominate over the radial components (see Figure 2 in J. S. Rankin et al. 2023), minimizing the influence of the radial discrepancy on ribbon ENA production.

The interstellar plasma/neutral temperature is 7500 K, and the flow speed is 25.4 km s^{-1} from the inflow direction (255.°7, 5.°1) in ecliptic J2000 coordinates (D. J. McComas et al. 2015). At the outer boundary of the LISM, the interstellar plasma density is 0.0856 cm^{-3} and the interstellar neutral H density is 0.11 cm^{-3} (see more details in E. J. Zirnstein et al. 2021b). As recent works have updated these densities (e.g., P. Swaczyna et al. 2020; F. Fraternale et al. 2023, 2024), we scale the proton density by treating the proton density in the heliospheric model as effective plasma density and assuming only $\sim$60% is proton (E. J. Zirnstein et al. 2021a); we scale the neutral H density by multiplying $\sim$1.7, referring to the pristine neutral H density $\sim$0.195 cm^{-3} in (P. Swaczyna et al. 2020). In our model, the density change could result in a difference in the simulated ribbon ENA intensity. A lower interstellar proton density would extend the spatial distribution of PINS further from the heliopause. The differential intensity of ENAs observed from a more distant source could decrease as the flux of the traveling ENAs becomes more diffuse. However, the decrease in ENA intensity might be moderated because fewer protons would reduce charge-exchange losses of ENA on their journey to IBEX and allow more ENA to be detected. A lower interstellar neutral H density would decrease the charge-exchange rate of the PINS so that the PINS can scatter more to approach isotropic distribution before converting to the secondary ENA, and therefore decrease the ribbon ENA

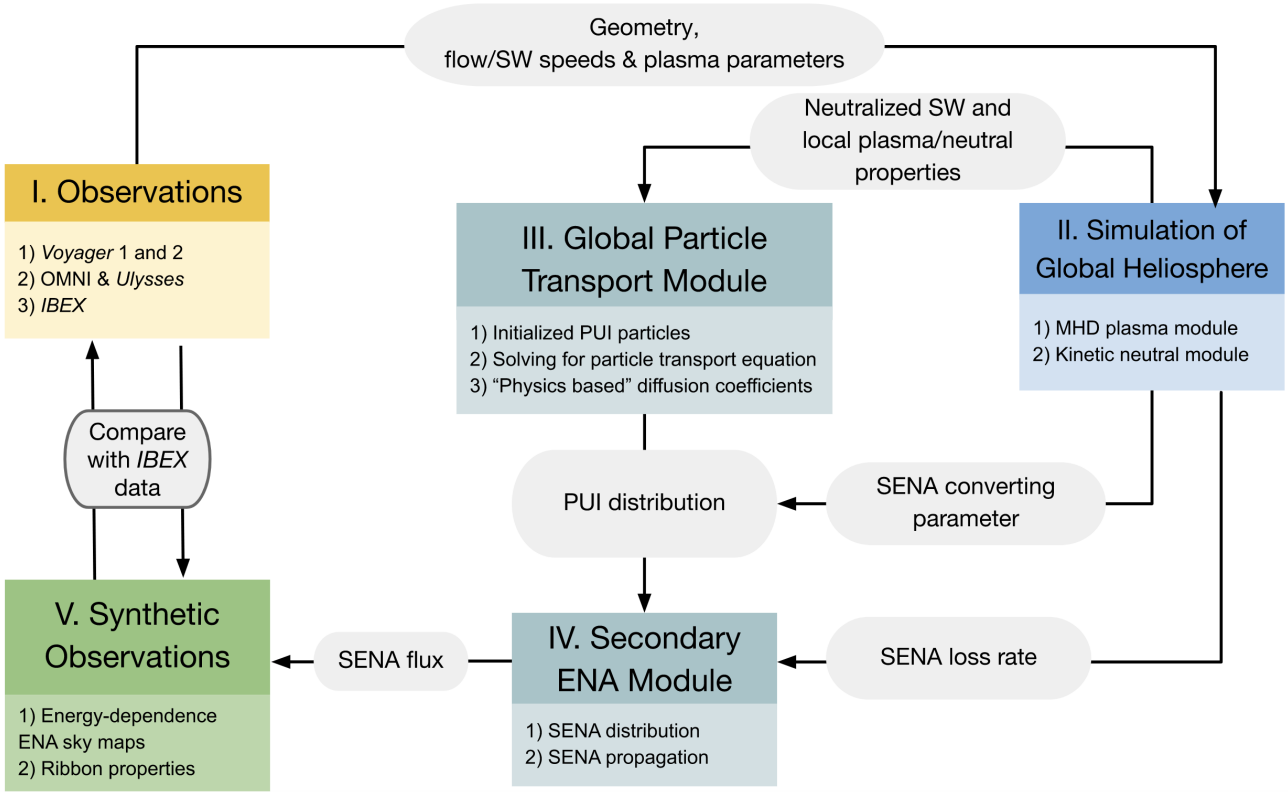

Figure 2. The flowchart of our numerical ribbon model. The background of the ribbon model is a three-dimensional MHD-plasma and kinetic-neutral simulation of SW–LISM interaction (box II), whose boundaries are derived from observations by IBEX, OMNI, and Ulysses (box I). The ribbon ENA simulation, with global particle transport module and secondary ENA module in boxes III and IV, respectively, is the main work in this paper. The particle transport module simulates the dynamics of PUIs, and the secondary ENA module computes the ENA production to produce synthetic observations of ribbon sky maps (box V), which is used to compare with the observations (box I).

intensity. In simulating the IBEX ribbon, the speculating method for the densities could be less appropriate than properly simulating the densities in the heliospheric MHD model. However, in this work, we are more focused on introducing a new numerical model for the IBEX ribbon and dynamics of PUIs outside the heliopause. The implementation of a more realistic global heliospheric MHD simulation in our model for reproducing the IBEX ribbon may be the subject of future work.

The SW information at 1 au is the same as the work of E. J. Zirnstein et al. (2021b), which is derived from a combination of measurements from the OMNI database at low latitudes and *Ulysses* measurements at high latitudes, averaged during 2004 to 2009. At high latitudes greater than 37°, the average SW properties at 1 au are the plasma speed of 743 km s^{-1}, the plasma density of 2.23 cm^{-3}, the temperature of 2.98×10^5 K, and the radial magnetic field component of 34.7 μG. At low latitudes less than 37°, the average SW plasma speed is 449 km s^{-1}, the plasma density is 6.53 cm^{-3}, the temperature is 1.02×10^5 K, and the radial magnetic field component is 37.4 μG. These values at 1 au are propagated to a distance at 10 au, which is the inner boundary of the global MHD simulation, by assuming adiabatic expansion. The simulation is performed with the coupled MHD and neutral code until a quasi-steady state is achieved (e.g., E. J. Zirnstein et al. 2021b).

Figure 3 shows the simulated heliosphere in simulation coordinates. The center is fixed at the Sun. The x–y plane is parallel to the solar equatorial plane, with $+x$-axis pointing in the direction from which the LISM flow comes (255.°7 in the ecliptic J2000 coordinates). The $+z$-axis aligns with the northern solar polar axis, and the $+y$-axis is oriented to complete the right-hand rule within the coordinate system. The Euler angles to rotate from the ecliptic J2000 to the simulation coordinates are (255.°7, −7.°3, −0.°7). The plotted domain range in each direction is from −500 to 500 au. In the left panel, we show the temperature of heliospheric structures. We can see two red tubes inside the HP that extend from the TS at high latitudes to the tail side as the fast SW is heated at the TS. The ISMF streamlines are draped around the heliosphere with a compressed magnetic field close to the HP. In the right panel, we show the HP as the isosurface of plasma density. The interstellar plasma flowing toward the heliosphere slows down slightly when moving toward the heliosphere and then accelerates around the HP.

2.2. Neutral Sources for PUIs beyond the Heliopause

The parent neutral population for PUIs outside the HP includes: (1) the neutral SW converted from the SW protons, (2) the interstellar pickup neutrals converted from interstellar PUIs generated in the radially propagating SW within the TS (N. A. Schwadron & D. J. McComas 2019; E. J. Zirnstein et al. 2023), and (3) the ENAs produced from hot ions in the IHS crossing the HP (J. Heerikhuisen et al. 2010; E. J. Zirnstein et al. 2013, 2016a). Our model currently considers NSW as the source of the ribbon (e.g., S. V. Chalov et al. 2010; J. Heerikhuisen et al. 2010; N. A. Schwadron &

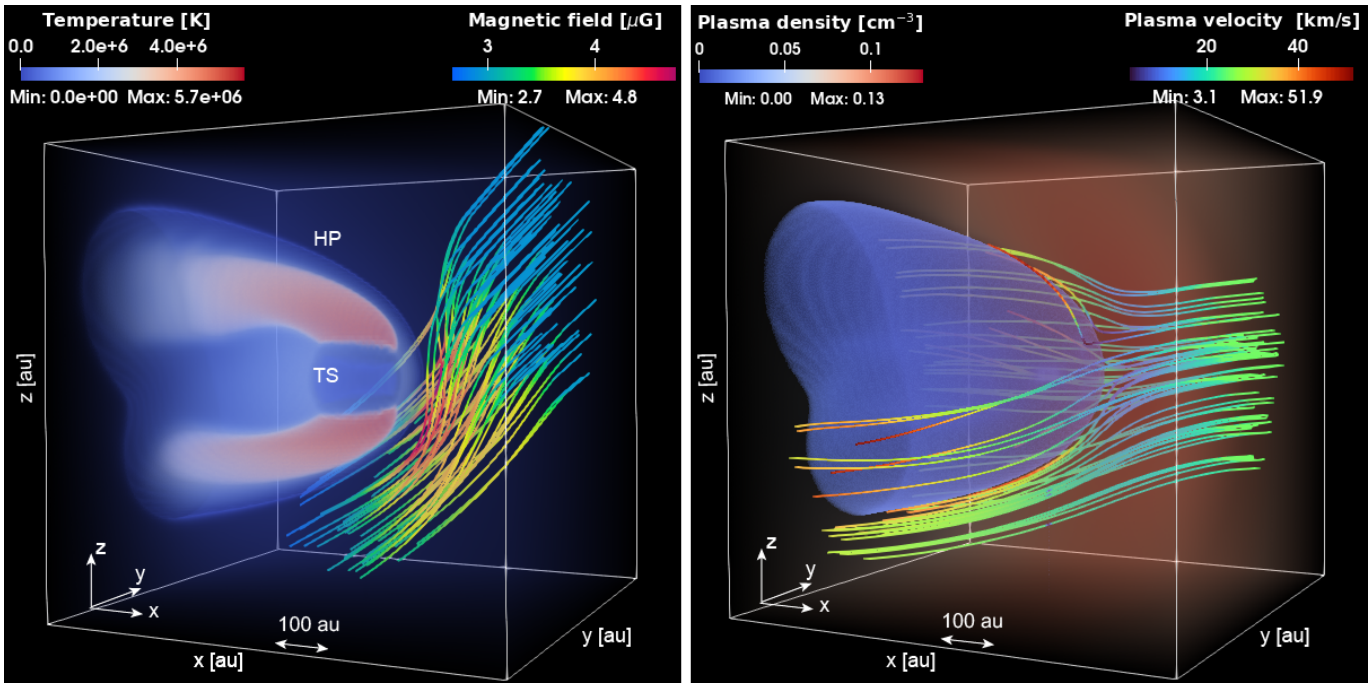

Figure 3. The visualization of the global heliospheric simulation results in the simulation coordinate system. The center is fixed at the Sun. The x–y plane is parallel to solar equatorial plane; $+x$-direction is at the same longitude as the LISM inflow direction (255.°7 in ecliptic J2000 coordinates). The $+z$-axis aligns with the northern solar polar axis, and the $+y$-axis is oriented to complete the right-hand rule within the coordinate system. The plotted domain range in each direction is from -500 au to 500 au. In the left panel, we show the ISMF streamlines and the temperature of the heliospheric structures. The right panel shows the flow velocity streamlines and the density distribution of the heliosphere.

D. J. McComas 2013; E. J. Zirnstein et al. 2013). The population of PUIs from the interstellar pickup neutrals and the heliosheath neutrals will be included in our future work.

In order to better simulate the ribbon, we utilize the NSW distribution as a function of heliographic latitude from a SW model derived from interplanetary scintillation (J. M. Sokół et al. 2015a; P. Swaczyna et al. 2016; E. J. Zirnstein et al. 2019). This NSW distribution enables us to achieve a higher resolution ($1.^{\circ}5 \times 3^{\circ}$) compared to the 6° resolution of the phase space distribution of neutral hydrogen within the global heliosphere simulation (J. Heerikhuisen et al. 2016). Given that the scale of the draped ISMF is significantly larger than the resolution in the global heliosphere model, utilizing the MHD simulation with a 6° resolution should be adequate. The SW speed and density at 1 au over the years from 2000 through 2009 are averaged to generate profiles at 1 au, $u_{\mathrm{SW},0}$, and $n_{\mathrm{SW},0}$, which are then used to calculate the differential flux of NSW, $I_{\mathrm{NSW}}(r_{\mathrm{TS}}, v, \theta)$, at the TS by integrating from 1 au to the TS (P. Swaczyna et al. 2016),

$$I_{\mathrm{NSW}}(r_{\mathrm{TS}}, v, \theta) = \frac{1}{M}\sum_{i=1}^{M}\int_{r_0}^{r_{\mathrm{TS}}} \times n_{\mathrm{SW},0}(\theta, i) u_{\mathrm{SW},0}(\theta, i)\left(\frac{r_0}{r_{\mathrm{TS}}}\right)^2 \times n_{\mathrm{H}}\sigma_{\mathrm{ex}}(v)\mathrm{e}^{-n_{\mathrm{H}}\sigma_{\mathrm{ex}}(v)r}\mathrm{N} \times (u_{\mathrm{SW},i}(r), \delta v|v) \times \frac{1}{m_p v} dr, \quad (1)$$

where v is the NSW speed, θ is the heliolatitude, i is the Carrington rotation number from 1958 through 2091 (total $M = 134$) corresponding to years 2000 to 2009, $r_0 = 1$ au, $n_{\mathrm{H}} = 0.127\ \mathrm{cm}^{-3}$ is the interstellar neutral H density inside the TS (P. Swaczyna et al. 2020), σ_{ex} is the cross section (B. G. Lindsay & R. F. Stebbings 2005), r is the radial distance from the Sun, m_p is the proton mass, and N is a Gaussian speed distribution with mean speed $u_{\mathrm{SW},i}(r)$ and speed variation $\delta v = 100\ \mathrm{km\ s}^{-1}$. Because the period 2000–2009 for NSW nearly covers solar cycle 23, the averaged NSW over this period approximately corresponds to the averaged IBEX observations in solar cycle 24 (D. J. McComas et al. 2014, 2020). In this work, we choose the period from 2009 to 2018 to average the observations, considering a predicted ∼4–9 yr delay between SW observations at 1 au and IBEX ribbon observations at 1 au (E. J. Zirnstein et al. 2015).

Assuming a radial expansion of the NSW, the differential flux at distance r from the Sun (beyond the heliopause) is (e.g., E. J. Zirnstein et al. 2020)

$$I_{\mathrm{NSW}}(\boldsymbol{r}, v, \theta) = I_{\mathrm{NSW}}(r_{\mathrm{TS}}, v, \theta)\left(\frac{r_{\mathrm{TS}}}{r}\right)^2 \exp \times \left(-\int_{r_{\mathrm{HP}}}^{r} n_p(\boldsymbol{r}')\sigma_{\mathrm{ex}} dr'\right), \quad (2)$$

where n_p is the interstellar plasma density from Section 2.1 and the term $\exp(-\int_{r_{\mathrm{HP}}}^{r} n_p(\boldsymbol{r}')\sigma_{\mathrm{ex}} dr')$ represents the loss by charge exchange beyond the heliopause. The PUIs from the NSW (hereafter PINS) source function can be calculated from $I_{\mathrm{NSW}}(r, v, \theta)$ as

$$S_{\mathrm{PINS}}(r, v, \theta) = \frac{I_{\mathrm{NSW}}(r, v, \theta)}{2\pi} m_p n_p(\boldsymbol{r})\sigma_{ex} v \times \left[\frac{1}{\pi\delta v_t^2(r)} e^{-\left(\frac{v_t}{\delta v_t(r)}\right)^2} H\left(\frac{\pi}{2} - \cos^{-1}(\hat{\boldsymbol{v}}_p \cdot \hat{\boldsymbol{r}})\right)\right], \quad (3)$$

$$v_t = v \cdot \sin(\cos^{-1}(\hat{\boldsymbol{v}}_p \cdot \hat{\boldsymbol{r}})), \tag{4}$$

$$\delta v_t(r) = \sqrt{\frac{2k_B T_{t,\mathrm{TS}}}{m_p}\left(\frac{r_{\mathrm{TS}}}{r}\right)^2}, \tag{5}$$

where the last term in square brackets of Equation (3) represents the transverse component of the NSW distribution based on the transverse temperature, which we set as 5×10^3 K at TS and drop off as r^{-2} due to expansion (V. Florinski & J. Heerikhuisen 2017). The Heaviside step function (H) is used to specify that PINS can only be created in the same hemisphere as the radially propagating NSW.

2.3. Global Particle Transport Module: Computing PUI Dynamics

2.3.1. The Governing Gyrophase-averaged Focused Transport Equation of PUIs

The most fundamental equation describing the motion of charged particles is the Newton–Lorentz equation. However, the gyroradius of the PUIs with a few keVs is $\sim 6 \times 10^4$ km in the LISM, which is much smaller than the scale of the heliosphere. Therefore, it is computationally expensive to track the full trajectories of PUIs across the entire ribbon region. In addition, as we have discussed, the anisotropy of the velocity distribution may be important for explaining the IBEX ribbon, so that it is appropriate to use the gyrophase-averaged focused transport equation, retaining the pitch-angle dependence of the distribution. The equation is also widely used in studies of the transport of solar energetic particles in the corona and interplanetary space (e.g., Y. Wang et al. 2012; M. Zhang & L. Zhao 2017; N. Wijsen et al. 2019; X. Kong et al. 2022) and particle acceleration at shocks (e.g., P. Zuo et al. 2011; J. A. le Roux & G. M. Webb 2012; Y. Y. Kartavykh et al. 2016).

The gyrophase-averaged focused transport equation for the distribution $f(\boldsymbol{x}, p, \mu, t)$ of PUIs as a function of spatial location $\boldsymbol{x}$, particle momentum p, pitch-angle cosine μ, and time t can be written as (E. C. Roelof 1969; J. Skilling 1975; G. M. Webb 1985; D. Ruffolo 1995; P. A. Isenberg 1997; G. Qin et al. 2004; M. Zhang 2006; M. Zhang et al. 2009; P. Zuo et al. 2011)

$$\frac{\partial f}{\partial t} = \nabla \cdot \kappa_\perp \cdot \nabla f - (v\mu\boldsymbol{b} + \boldsymbol{U} + \boldsymbol{V_d}) \cdot \nabla f + \frac{\partial}{\partial \mu} D_{\mu\mu} \frac{\partial f}{\partial \mu} - \frac{d\mu}{dt}\frac{\partial f}{\partial \mu} - \frac{dp}{dt}\frac{\partial f}{\partial p}, \tag{6}$$

$$\frac{d\mu}{dt} = \frac{1-\mu^2}{2}\left[-\frac{v}{L_B} + \mu(\nabla \cdot \boldsymbol{U} - 3\boldsymbol{bb}\colon \nabla \boldsymbol{U})\right], \tag{7}$$

$$\frac{dp}{dt} = -p\left[\frac{1-\mu^2}{2}(\nabla \cdot \boldsymbol{U} - \boldsymbol{bb}\colon \nabla \boldsymbol{U}) + \mu^2 \boldsymbol{bb}\colon \nabla \boldsymbol{U}\right], \tag{8}$$

where the terms on the right-hand side of Equation (6) are cross-field spatial diffusion with coefficient $\kappa_\perp$ (J. R. Jokipii 1966), streaming along the ambient magnetic field $\boldsymbol{B} = B\boldsymbol{b}$ with speed v and pitch-angle cosine μ, advection with plasma flow $\boldsymbol{U}$, particle drift $\boldsymbol{V_d}$, pitch-angle diffusion with a coefficient $D_{\mu\mu}$, pitch-angle change due to focusing, and momentum gain/loss, respectively. The $\boldsymbol{V_d}$ is written as (T. G. Northrop 1963)

$$\boldsymbol{V_d} = \frac{cpv}{qB}\left[\frac{1-\mu^2}{2}\frac{\boldsymbol{B} \times \nabla B}{B^2} + \mu^2 \frac{\boldsymbol{B} \times [(\boldsymbol{B} \cdot \nabla)\boldsymbol{B}]}{B^3} + \frac{1-\mu^2}{2}\frac{\boldsymbol{B}(\boldsymbol{B} \cdot \nabla \times \boldsymbol{B})}{B^3}\right], \tag{9}$$

where c is the light speed and q is the charge of particles. The terms in the change in pitch angle, Equation (7), take into account the focus on the nonuniform magnetic field with a focal length $L_B = (\boldsymbol{b} \cdot \nabla \ln B)^{-1}$, and changes in pitch angle due to an anisotropic adiabatic momentum change. The momentum change term shown in Equation (8) is adiabatic cooling/heating. Note that the transport equation is written with variables in mixed reference frames, with momentum and pitch angle in the plasma "coflowing" frame and the spatial coordinates in the fixed reference frame.

Because the speed of high-energy PUIs is much greater than the propagation speed of magnetic field turbulence in the interstellar medium, which is typically the Alfvén speed or fast-mode MHD wave speed, magnetic field fluctuation dominates all the diffusion. In this case, the diffusion terms related to p disappear as the electric field fluctuation can be treated as zero, $\delta \boldsymbol{E} = 0$ (M. Zhang 2006), and the remaining nonzero diffusion coefficients are pitch-angle diffusion $D_{\mu\mu}$ and cross-field diffusion $\kappa_\perp$.

Since the transport equation is essentially a Fokker–Planck equation, it is mathematically equivalent to a set of time-forward stochastic differential equations (SDEs; e.g., M. Zhang 1999; X. Li et al. 2018, 2022; X. Kong et al. 2022). The corresponding SDEs can be written as

$$d\boldsymbol{X} = (v\mu\boldsymbol{b} + \boldsymbol{U} + \boldsymbol{V_d} + \nabla \cdot \kappa_\perp)dt + \sqrt{2\kappa_\perp} \cdot d\boldsymbol{W}_x(t), \tag{10}$$

$$dp = \frac{dp}{dt}dt, \tag{11}$$

$$d\mu = \left[\frac{d\mu}{dt} + \frac{\partial D_{\mu\mu}}{\partial \mu}\right]dt + \sqrt{2D_{\mu\mu}}\,dW_t(t), \tag{12}$$

where $d\boldsymbol{W}_x(t)$ and $dW_t(t)$ are Wiener processes.

2.3.2. The Diffusion Coefficients

Given that our purpose of this work is to study how the change in the diffusion coefficients, $D_{\mu\mu}$ and $\kappa_\perp$, of the PUIs outside the HP affects the properties of the ribbon, we treat the coefficients as free parameters. We assume that the coefficients are uniform for simplicity. To calculate "free" $D_{\mu\mu}$ and $\kappa_\perp$ used in our model, we artificially choose the parallel mean free path, λ, of the PUIs at 1 keV and calculate $D_{\mu\mu}$ and $\kappa_\perp$ accordingly. In the rest of this paper, the parallel mean free path is referred to as that of PUIs at 1 keV, unless otherwise specified.

With the definition, $\lambda = 3\kappa_\parallel/v$, we can easily have the spatial diffusion coefficient along the ambient magnetic field, $\kappa_\parallel$. According to the quasi-linear theory, $\kappa_\parallel$ can be related to $D_{\mu\mu}$ by (e.g., J. R. Jokipii 1966)

$$\kappa_\parallel(v) = \frac{v^2}{4}\int_0^1 \frac{(1-\mu^2)^2}{D_{\mu\mu}}d\mu. \tag{13}$$

To calculate $D_{\mu\mu}$, which is μ dependent, we take the form of (G. Qin et al. 2005; M. Zhang & L. Zhao 2017; X. Kong et al. 2022):

$$D_{\mu\mu} = D_0(1 - \mu^2)\left(\frac{p}{p_0}\right)^{\Gamma-1}(|\mu|^{\Gamma-1} + h_0). \quad (14)$$

This form estimates the particle scattering in the magnetic field turbulence power-law spectrum of slope $-\Gamma$ in the nonrelativistic limit according to the quasi-linear theory. For a Kolmogorov spectrum, $\Gamma = 5/3$. The parameter h_0 is added to describe the scattering through $\mu = 0$ by nonresonant scattering or nonlinear effects, and we set $h_0 = 0.2$ according to M. Zhang & L. Zhao (2017). p_0 is the momentum of the reference particle at 1 keV. D_0 is treated as a location-independent factor that needs to be calculated according to the assumed mean free path. For 1 keV PUIs, $p/p_0 = 1$, by putting Equation (14) into Equation (13), we have $D_0 = 0.83985v_0/\lambda$. Therefore, $D_{\mu\mu}$ is

$$D_{\mu\mu} = \frac{0.83985v_0}{\lambda}(1 - \mu^2)\left(\frac{p}{p_0}\right)^{\frac{2}{3}}(\mu^{\frac{2}{3}} + 0.2), \quad (15)$$

and $\kappa_\parallel$ is

$$\kappa_\parallel = \kappa_{\parallel 0}\left(\frac{p}{p_0}\right)^{\frac{4}{3}}, \quad (16)$$

where $\kappa_{\parallel 0} = \lambda v_0/3$. For the perpendicular diffusion coefficient $\kappa_\perp$, we take $\kappa_\perp/\kappa_\parallel = 0.01$, which is similar to the results of the test-particle simulations in synthetic turbulence (J. Giacalone & J. R. Jokipii 1999). In general, the ratio of $\kappa_\perp/\kappa_\parallel$ is reduced in the case of weaker turbulent scattering. However, because the details of the turbulence outside the HP are unknown and beyond the scope of this paper, for simplicity, we fix the ratio as 0.01 in all simulations of this paper.

2.3.3. Initialization of Pseudoparticles for PINS

We use pseudoparticles in SDEs to represent and model the dynamics of PUIs. The amount of real particles that a PINS pseudoparticle represents, the weight w, is written as

$$w = \frac{\int_{V_x}\int_{V_v} f_{\mathrm{PINS},\delta t}\, d^3\boldsymbol{x} d^3\boldsymbol{v}}{N_m}, \quad (17)$$

where $f_{\mathrm{PINS},\delta t}$ is the distribution of PINS created during δt, $f_{\mathrm{PINS},\delta t} = \delta t S_{\mathrm{PINS}}$ (note that S_{PINS} is the source function of PINS in Section 2.2), N_m is the number of pseudoparticles (in this work we set $N_m = 10^8$) initialized in the volume of velocity space, V_v, and the volume of Cartesian space, V_x. The position and velocity of each pseudoparticle are determined according to the distribution, $f_{\mathrm{PINS},\delta t}$. We only initialize pseudoparticles beyond the HP, whose location is determined by a temperature threshold of 10^5 K.

2.4. SENA Module: Computing the SENA Differential Intensity Detected by IBEX

Because our model is time independent, we treat the PINS population as a steady state so that the SENA production from PINS is equal to the PINS production from NSW during δt, written as

$$\int_{V_x}\int_{V_v} f_{\mathrm{SENA},\delta t}\, d^3\boldsymbol{x} d^3\boldsymbol{v} = \int_{V_x}\int_{V_v} f_{\mathrm{PINS},\delta t}\, d^3\boldsymbol{x} d^3\boldsymbol{v}, \quad (18)$$

where $f_{\mathrm{SENA},\delta t}$ is the distribution of SENA converted from PINS during δt and $f_{\mathrm{PINS},\delta t}$ is the distribution of PINS converted from NSW during δt. In our SENA module, the PINS population gradually converts to SENA due to charge exchange along their trajectories. The strategy for computing $f_{\mathrm{SENA},\delta t}$ is to accumulate the distributions of newly created SENA along the trajectory of each PINS pseudoparticle. To calculate the differential intensity of the ENA in the ribbon sky maps, we only need to select the SENA within $f_{\mathrm{SENA},\delta t}$ that can be observed by the IBEX. The details are provided below.

The SENA differential intensity detected by IBEX, j, which means ENA counts detected, δN, per unit area, δA, per unit time interval, δt, per unit solid angle, $\delta\Omega$, per unit energy interval, δE, can be written as

$$j = \frac{\delta N}{\delta\Omega\delta A\delta t\delta E}. \quad (19)$$

We assume that a pseudoparticle with weight, ω, moves to a position $\boldsymbol{r}$ at time t ($t = 0$ means the time when the pseudoparticle is initialized) and is converted to SENA of amount N. Therefore, N can be written as

$$N = wW(t)\, dt, \quad (20)$$

where dt is the time step along the trajectory and $W(t)$ is the weighting function that the pseudoparticle can contribute to creating SENA at time t, written as (E. J. Zirnstein et al. 2015)

$$W(t) = \frac{e^{-t/\tau_{ex}}}{\int_0^{t_{max}} e^{-t'/\tau_{ex}} dt'}, \quad (21)$$

where τ_{ex} is the charge-exchange mean free lifetime as $\tau_{\mathrm{ex}} = \eta^{-1}$ and η is the converting rate that is a function of neutral H density n_{H}, cross-section σ_{ex}, and PINS speed v_i, as $\eta = n_{\mathrm{H}}\sigma_{\mathrm{ex}}v_i$, and t_{max} is the total lifetime that is set as $t_{\mathrm{max}} = 3\tau_{\mathrm{ex}}$. It is easy to see that the integral of $W(t)$ from $t = 0$ to t_{max} equals 1.

Since the pitch angle of one PINS pseudoparticle is a single value, to determine feasibly whether the newly created SENA can be detected, we assume that the PINS pseudoparticles have a small but finite amount of opening angle ($\Delta\psi$) around the nominal pitch angle (ψ). In this work, we make $\Delta\psi = 1°$. If the small opening angle of the PINS pseudoparticle intersects the LOS of IBEX, the newly created SENA can be detected. We use a factor $P = 1$ to represent the detection, otherwise $P = 0$. We define Ω as the solid angle of the newly created SENA propagating from the position of the pseudoparticle $\boldsymbol{r}$, written as $\Omega = 2\pi[\cos(\psi - \Delta\psi/2) - \cos(\psi + \Delta\psi/2)]$. Therefore, the detected SENA counts per unit area contributed from one pseudoparticle at time t is calculated as

$$\frac{\delta N}{\delta A} = P\frac{N}{A} = P\frac{wR(t)}{A}, \quad (22)$$

where $R(t) = W(t)dt$ and $A = r^2\Omega$.

The solid angle observed by IBEX is $\Omega_{ob} = \sin\theta\Delta\theta\Delta\varphi$ in which θ and φ are latitude and longitude, respectively. We choose the angular resolution $\Delta\theta\Delta\varphi = 2° \times 2°$ in our model.

Therefore, at time t, the PINS pseudoparticle, i, contributes to the ENA differential intensity at energy E of the pixel (θ, φ) by

$$j_i(E, t) = \frac{\delta N}{\delta A \delta \Omega \delta E \delta t} = P \frac{wR(t)}{A\Omega_{ob}\delta E \delta t}, \quad (23)$$

where δE is the energy interval. Note that the weight of the PINS pseudoparticles, ω, is defined for PINS created in a time interval δt, and therefore, δt in Equation (23) is canceled. By accumulating Equation (23) for all pseudoparticles at each time step during their lifetimes, we can compute the ENA differential intensity at energy E as

$$J(E) = \sum_{i,t} j_i(E, t). \quad (24)$$

For the differential intensity at the central energy of each passband k of IBEX-Hi (H. O. Funsten et al. 2009b), $J(E_k)$, we implement an energy response function, $F(E)$, and integrate over the energy passband so that the differential intensity for each passband is written as

$$J(E_k) = \int_k J(E) F(E). \quad (25)$$

3. Simulation Results

In this section, we present simulation results of the ENA differential intensities detected at 1 au in cases with different PUI parallel mean free paths and compare them with observations. To study the effects of scattering on ribbon properties, we show the center position of the ribbon, the profiles of the ribbon ENA intensity in the ribbon-centered frame at several azimuthal slices, and the spatial distribution of ribbon ENA production.

We compare the simulation results with the Compton–Getting and survival-probability corrected "Theseus" maps for the IBEX-Hi ENA data after ribbon separation. Theseus (D. Osthus et al. 2023) is a new map-rendering method of the IBEX data that takes the input of 1 degree binned count rate data of ENA and uses a statistically rigorous two-dimensional surface estimation technique, including a deconvolution of the IMAP-Hi angular response function (FWHM of $6.^{\circ}5$) to model the IBEX data, leading to maps of significantly increased spatial resolution ($2^{\circ} \times 2^{\circ}$). The method of separating the ribbon from the globally distributed flux (GDF) is described in L. J. Beesley et al. (2023). It first applies an image edge detection method to identify the ribbon region on the map and then predicts the contribution of the GDF under the ribbon. Their new ribbon separation minimizes assumption-driven biases in the resulting separation, e.g., it does not constrain the ribbon to follow a specific analytic form (e.g., Gaussian, kappa distribution, see more details in L. J. Beesley et al. 2023), so that the resulting ribbon shape provides a better representation of the true ribbon structure present in the data. S. J. Noh et al. (2025) have a detailed analysis of the ribbon properties with this data set.

3.1. Sky Maps of ENA Differential Intensity

Figure 4 shows ENA differential intensity synthetic sky maps for each energy passband of IBEX-Hi for different parallel mean free paths of 500, 1000, 2000, and 5000 au, respectively, and the IBEX data averaged from 2009 to 2018. In the low-energy passbands, 0.71 keV (ESA 2) and 1.11 keV (ESA 3), the maximum intensity is at low latitudes ($\lesssim 30^{\circ}$), which is indicative of the neutralized slow SW ($\sim$350 $-$450 km s^{-1}) near the equatorial plane. In ESA 3, the maximum intensity regions (second row, dark red regions) are slightly apart from the equatorial plane compared to ESA 2. This is consistent with the fact that the SW particles with higher energy are generally coming from higher latitudes. In the higher-energy passbands, 1.74 keV (ESA 4), 2.73 keV (ESA 5), and 4.29 keV (ESA 6), the ribbon clearly has two lobes, which is consistent with the presence of neutralized fast SW ($\gtrsim$550 km s^{-1}) at high latitudes.

For each energy passband, as the mean free path increases, the ribbon has a higher intensity and a narrower structure. For example, in ESA 4, the ribbon in the case with $\lambda = 5000$ au has a peak intensity about 50 (cm^2 s sr keV)$^{-1}$, while it is about 20 (cm^2 s sr keV)$^{-1}$ in the case with $\lambda = 500$ au. In addition, the ribbon in the case with $\lambda = 5000$ au is significantly narrower than that in the case with $\lambda = 500$ au. Because a longer mean free path corresponds to weaker pitch-angle scattering, and therefore to a more anisotropic velocity distribution of PUIs, the region where ENA can be detected along the LOS is narrower and the observed ENA intensity is higher.

Compared with the Theseus data, our simulation results show a ribbon similar to the observations, but with some noticeable differences. For instance, in ESA 2 and ESA 3, the brightest region of the observed ribbon is at a latitude of about -30° south, whereas the ribbon intensity peaks nearer to the equatorial plane in the simulations. The main reason for the difference is that the NSW data we used in this work were averaged from 2000 through 2009, which was shown to have no significant large flux of NSW at a latitude of approximately -30° in the south, but was distributed mainly at latitudes from -10° to 20° for 0.71 keV (ESA 2) and from -40° to 40° for 1.11 keV (ESA 3) (see Figure 1 in E. J. Zirnstein et al. 2020). The features of the NSW data are consistent with our simulation results of the ribbon in ESA 2 and ESA 3, in which the maximum intensity is around the equatorial plane. However, the annual ENA maps, shown in Figure 7 of D. J. McComas et al. (2024), reveal that the brightest regions, especially in the maps from 2009 to 2012, are in the south of the ribbon. The difference may indicate that using the averaged NSW data over nearly a solar cycle cannot reproduce some detailed features in the sky maps over a timescale of a few years. In the future, we will attempt to implement neutral source models based on time-dependent NSW data to better compare with the IBEX observations (E. J. Zirnstein et al. 2023). In the high-energy passbands of ESA 5 and ESA 6, the peak intensity of the ribbon, even in the weakest scattering case with $\lambda = 5000$ au, is significantly lower than that in the observations. This is mainly because the ribbon ENA source in our model did not consider interstellar pickup atoms in the SW, which dominate the $\sim$2–6 keV range of the ENA emission.

For ESA 4, the case with $\lambda = 5000$ au, which is more consistent with the weakly scattering scenario, has the most comparable peak intensity ($\sim$50 (cm^2 s sr keV)$^{-1}$) to the observed ribbon. The peak intensity in the observation is at a higher latitude by $\sim 10^{\circ}$ in the north than that in the case with $\lambda = 5000$ au, and the intensity in the south of the ribbon observation ($\sim$40 (cm^2 s sr keV)$^{-1}$) is slightly greater than in the case with $\lambda = 5000$ au ($\sim$35 (cm^2 s sr keV)$^{-1}$). Based on the comparison of the peak intensity in passbands of ESA 2, 3,

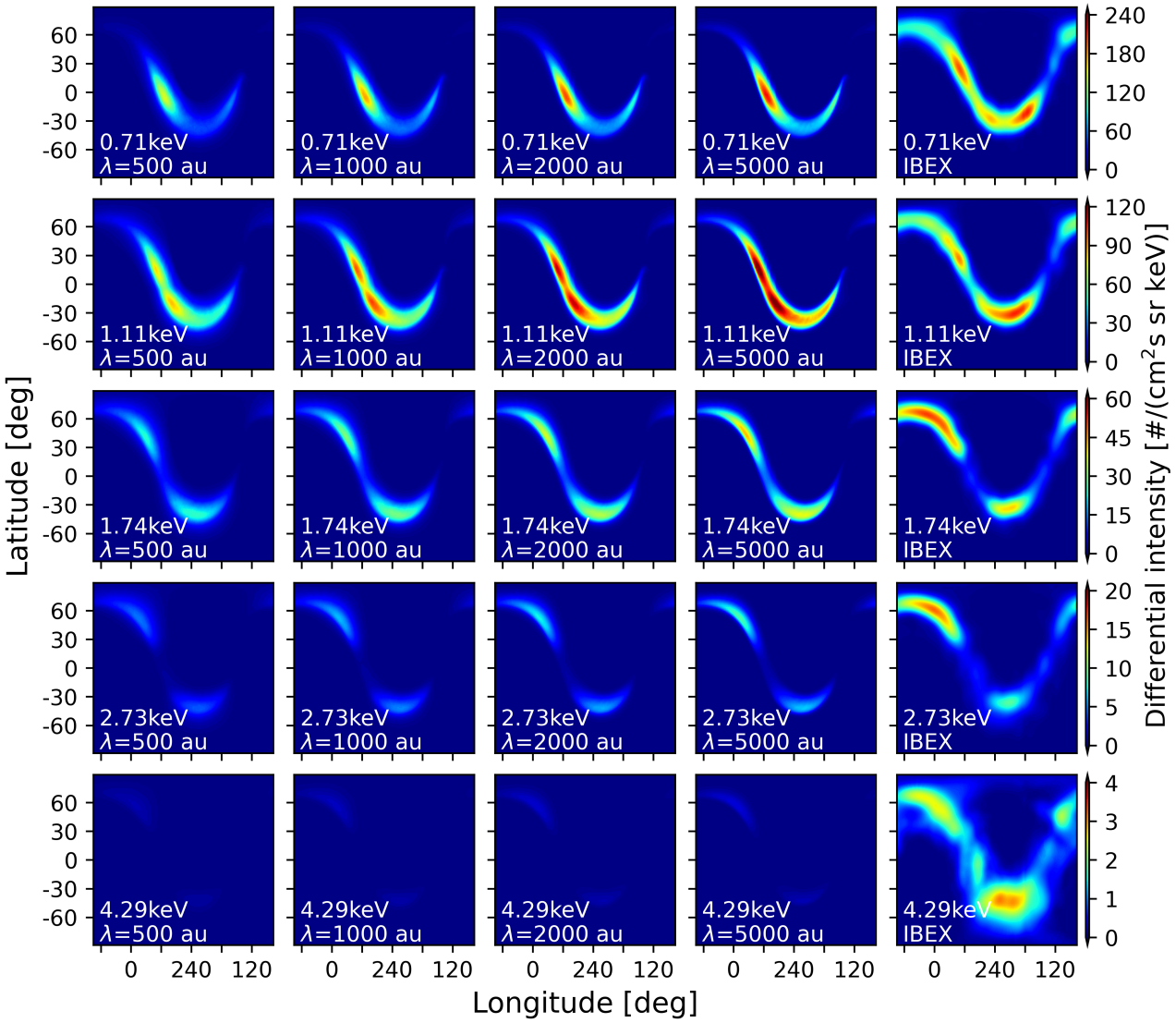

Figure 4. The ENA differential intensity synthetic sky maps with parallel mean free paths 500 au, 1000 au, 2000 au, and 5000 au for 0.71 keV (ESA 2), 1.11 keV (ESA 3), 1.74 keV (ESA 4), 2.73 keV (ESA 5), and 4.29 keV (ESA 6), respectively, and the IBEX data averaged from year 2009 to 2018.

and 4, we can estimate that the mean free path is on the order of several thousand au.

As mentioned above, the NSW data used in the simulation could significantly affect the simulated ribbon ENA intensity and cause the difference between simulations and observations. We can see that the simulation in ESA 4 has the best agreement with the observation. This happens because this energy passband (1.74 keV) contains mostly the high-speed component of the NSW, which is strongest at solar minimum and at high northern and southern latitudes, and it is below the energy range where interstellar pickup atoms significantly contribute. Therefore, in the remainder of Section 3, we focus mainly on ESA 4 when comparing our simulations with the observations.

3.2. Ribbon Center

In Figure 5, we plot ribbon ENA sky maps at 1.74 keV (ESA 4) for the IBEX data and for the simulation cases with $\lambda =$ 500 au, 1000 au, 2000 au, and 5000 au, respectively, centered at the ecliptic J2000 (longitude, latitude) = (227.°28, 34.°62), which is the pristine ISMF direction ($\boldsymbol{B}_\infty$) used in our model. The nose direction is located at an azimuth angle equal to 0. The ribbon ENA emission is within the polar angle range of 60°–90°. The ribbon centers, marked as "RC" (white for IBEX data and red for simulations) in each panel, are calculated through a circular fit (white dashed line for IBEX data and red dashed lines for simulations) of ENA intensity peaks (black circles) in each meridian slice, whose resolution is 2°. Figure 5 shows that the ribbon center for the IBEX data shifts several degrees (∼6°) away from the $\boldsymbol{B}_\infty$ direction. Because the draped ISMF is nearly symmetric to the $\boldsymbol{B}_\infty - \boldsymbol{V}_\infty$ plane, the ribbon center is still quite close to the $\boldsymbol{B}_\infty - \boldsymbol{V}_\infty$ plane (with a difference of $\lesssim$2°), where $\boldsymbol{V}_\infty$ is the LISM plasma inflow direction. The ribbon centers in the simulation cases are closer to the $\boldsymbol{B}_\infty$ direction used in the simulation than the IBEX data. The difference can be recognized from the fitted circle of the IBEX ENA intensity peaks, shown as the white dashed circles, which extend further tailward than the fitted red dashed circles.

Figure 6 shows the ribbon centers in ecliptic J2000 coordinates as a function of energy for the IBEX data and

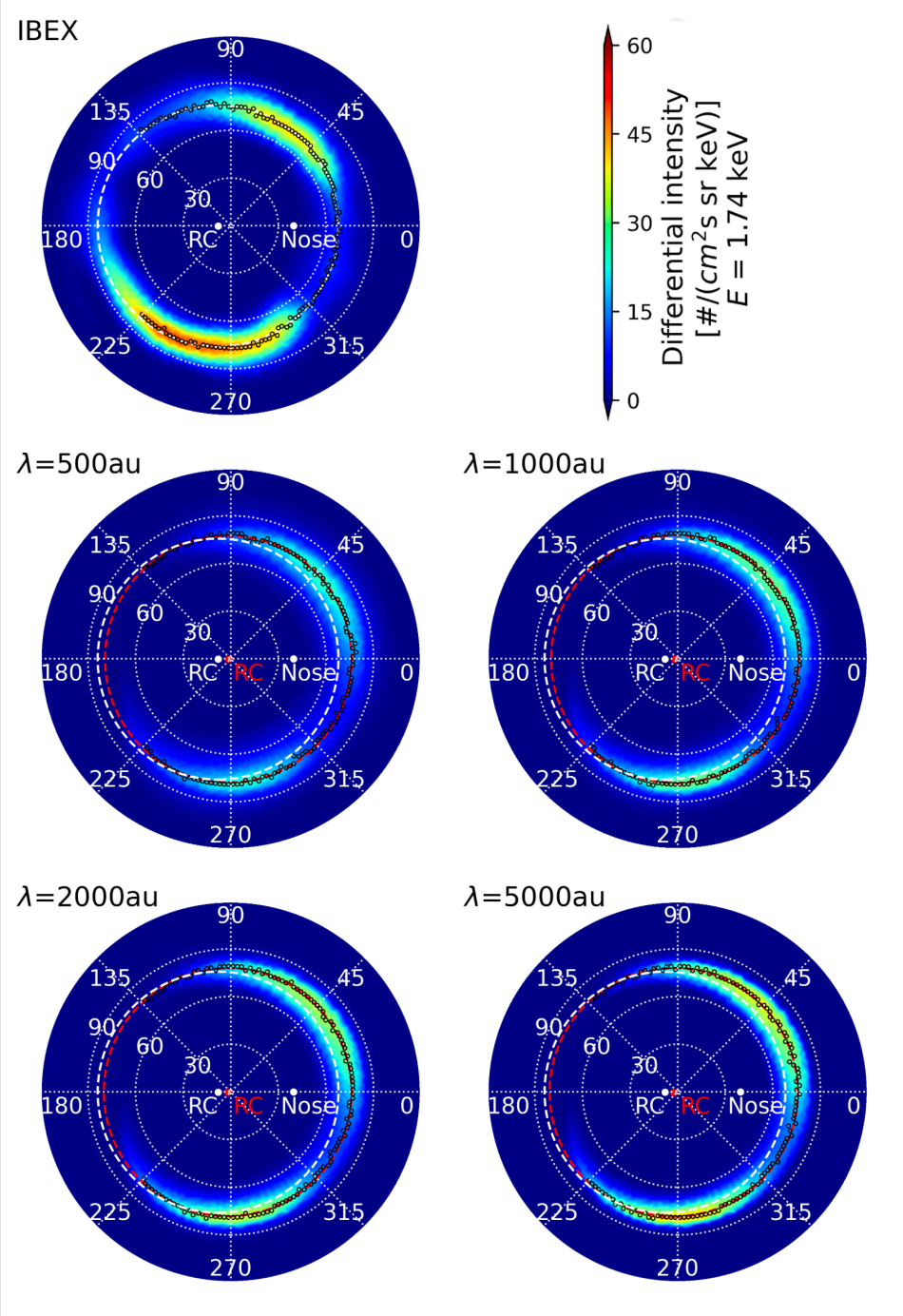

Figure 5. The ENA differential intensity sky maps in the ribbon-centered frame for ESA 4 (1.74 keV) are presented for IBEX data averaged over the years 2009 to 2018, and for simulation cases with parallel mean free paths λ = 500, 1000, 2000, and 5000 au, respectively. The maps are centered at (longitude = 227.°28, latitude = 34.°62) in J2000 ecliptic coordinates, and the nose positions (white dots marked as "Nose") are located at azimuthal angle (ϕ) equals 0. The ribbon centers, marked as "RC" (white for IBEX data and red for simulations) in each panel are calculated via a circular fit (white dashed line for IBEX data and red dashed lines for simulations) of ENA intensity peaks (black circles) in each meridian slice, whose azimuthal resolution is 2°.

for the simulation cases with mean free paths $\lambda = 500$ au, 1000 au, 2000 au, and 5000 au, respectively. The mean center is weighted over energies, as was done by E. J. Zirnstein et al. (2016b). Our results show that with stronger scattering, going from $\lambda = 5000$ au to $\lambda = 500$ au, the ribbon centers of the low-energy channels shift more to the east of the mean center, while the ribbon centers of the high-energy channels shift more to the south. Note that in the plots of Figure 6, the left direction is eastward and the right direction is westward.

We can also see that there is a southward shift of the ribbon centers from the low-energy channel to the high-energy channel, which is consistent with the findings of M. A. Dayeh et al. (2019). The southward shift (see also P. Swaczyna et al. 2016) is explained by the structure of the heliosphere (e.g., D. B. Reisenfeld et al. 2021) and the SW (e.g., M. A. Dayeh et al. 2011; J. M. Sokół et al. 2015b) that results in a different contribution of the fast SW at northern and southern high latitudes. Since the position of the ribbon in

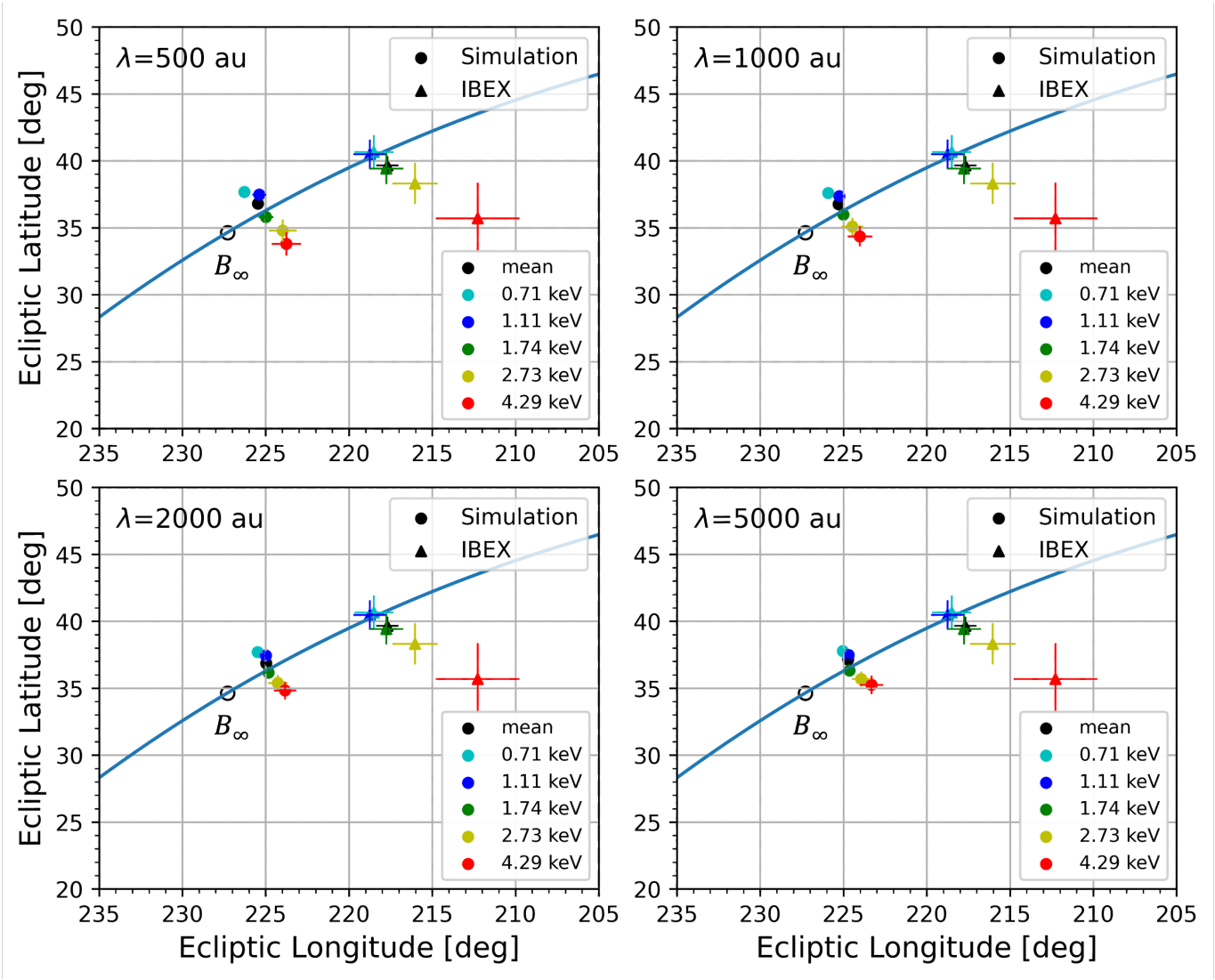

Figure 6. Ribbon centers in the ecliptic J2000 coordinates for IBEX data and for the simulation cases with mean free paths λ = 500, 1000, 2000, and 5000 au, respectively. The black circles, marked as B_∞, are the direction of the local ISMF in our simulations. The solid blue line shows the $\boldsymbol{B}_\infty - \boldsymbol{V}_\infty$ plane, where $\boldsymbol{V}_\infty$ is the LISM plasma inflow direction.

the southern hemisphere lies approximately 39° (M. A. Dayeh et al. 2019) further from the southern heliospheric pole compared to that in the northern hemisphere, the high-energy ENAs produced by the fast SW near the southern pole are more likely to populate the outer edge of the ribbon in the southern hemisphere (i.e., the side closer to the southern pole). In contrast, the ENAs produced by the fast SW near the northern pole contribute similarly to the inner and outer edges of the ribbon in the northern hemisphere. Therefore, the asymmetry of the fast SW contribution shifts the overall ribbon structure southward. Additionally, since secondary ENAs with higher energy are formed farther from the heliosphere and the draped magnetic field unfolds with increasing distance from the HP (see Section 3.3; see also E. J. Zirnstein et al. 2015), the ENA emissions at higher energies from the fast SW are more likely to move toward the outer edge. Thus, the asymmetry of the draped ISMF in the south and north due to the structure of the heliosphere likely leads to a net southward shift of the ribbon with increasing energy.

Compared with the ribbon centers calculated by E. J. Zirnstein et al. (2016b), Figure 6 shows that the ribbon centers of our simulation are closer to $\boldsymbol{B}_\infty$. The difference may arise because our simulation solves for the transport of the PUIs (see Section 2.3), whereas E. J. Zirnstein et al. (2016b) impose a predefined PUI distribution in the form of a partial shell. The difference could result in a different spatial distribution of ENA emission. Since the PUI distribution varies under different PUI transport scenarios, our ribbon model, with the ability to incorporate the PUI transport into global ribbon modeling, can provide insights into identifying the most reasonable transport scenario by comparing with observations.

3.3. Ribbon Intensity Profile at Azimuthal Slices

To study the effects of the PUI scattering on the properties of the simulated ribbon cross-sectional profiles, Figure 7 shows the ENA differential intensity for 1.74 keV (ESA 4) as a function of the polar angle from the intensity peak for several azimuthal slices (Figure 5). In the simulations, the polar angular distance

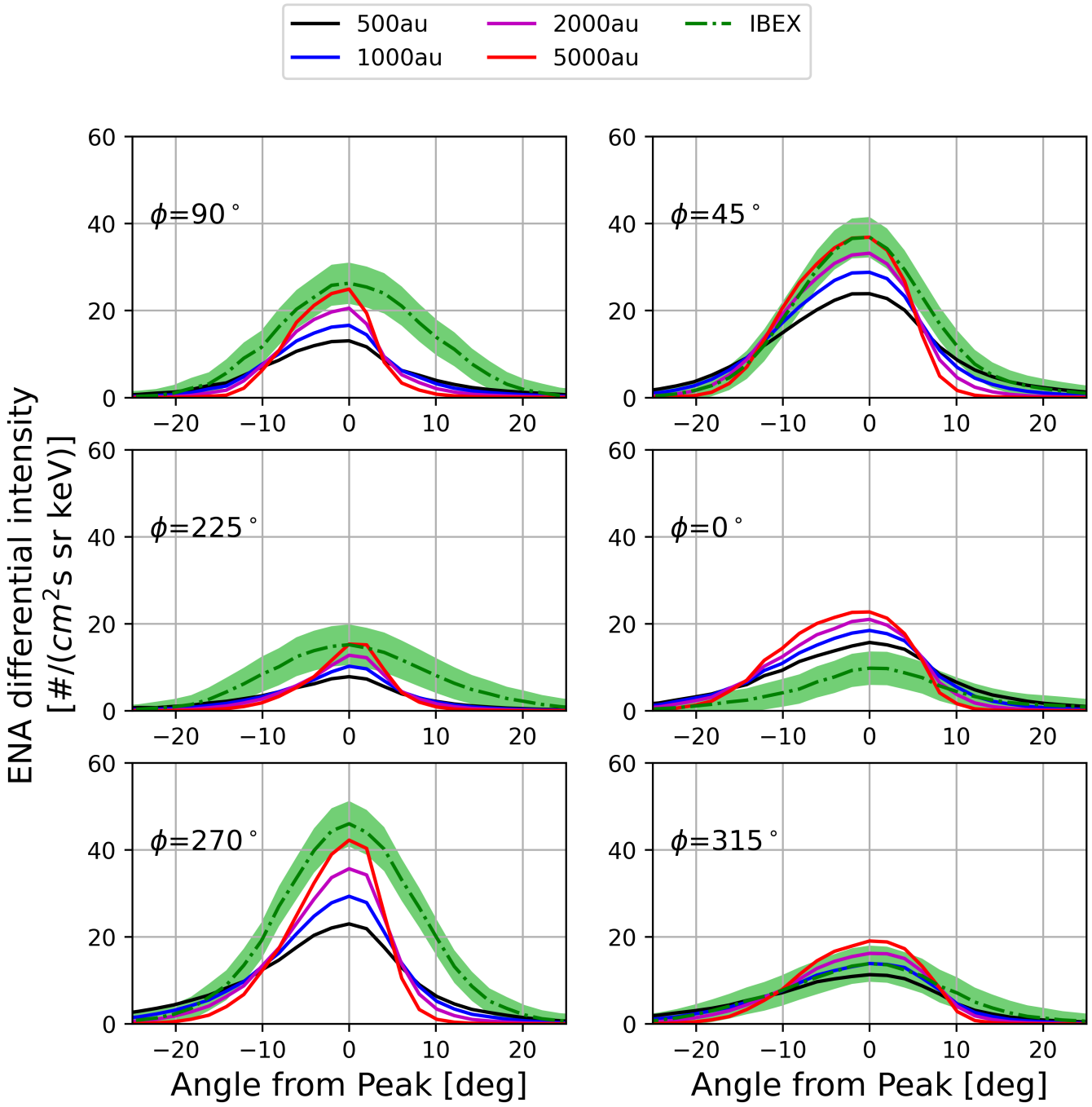

Figure 7. ENA differential intensity for 1.74 keV as a function of the angle from the peak at several azimuthal cuts with angle ϕ in Figure 5. The solid lines show the simulation results, and the dotted–dashed lines with error bars ($\pm 1\sigma$) show the observation. The ribbon center is to the left of each panel.

of the peaks from the ribbon centers at each azimuthal slice varies by $\lesssim 2^\circ$ in the cases with different λ. However, the polar angle of the peaks in the observations could be significantly different. For example, at the $\phi = 0^\circ$ slice of Figure 5, the peaks of the observation are $\sim 10^\circ$ closer to the ribbon center than the simulations. Matching the observed peak locations relative to the RC is not our main objective; therefore, we coalign the peaks of the ribbon intensities in Figure 7 to focus on the change in the width of the ribbon and the profile asymmetry at the inner and outer edges.

In general, as the mean free path increases, the intensity peak becomes higher and narrower. For example, for the slice at $\phi = 270^\circ$, the intensity of the peak decreases from ~ 42 to ~ 23 (cm^2 s sr keV)$^{-1}$, and the FWHM increases from $\sim 13^\circ$ to $\sim 19^\circ$. This feature is consistent with the fact that with stronger pitch-angle scattering, the PUI distribution is more isotropic, and therefore the ribbon intensity is lower and the width is wider (see also Figure 8, showing that the ribbon source region is more concentrated with increasing mean free path). Figure 7 shows that the ENA peak intensity in the case for $\lambda = 5000$ au is the most comparable to the observations, especially for the slices with the brightest ENA emissions ($\phi = 45^\circ$ and 270°). However, our simulations at $\phi = 0^\circ$ show a substantial overestimation compared to the observed ribbon intensity,

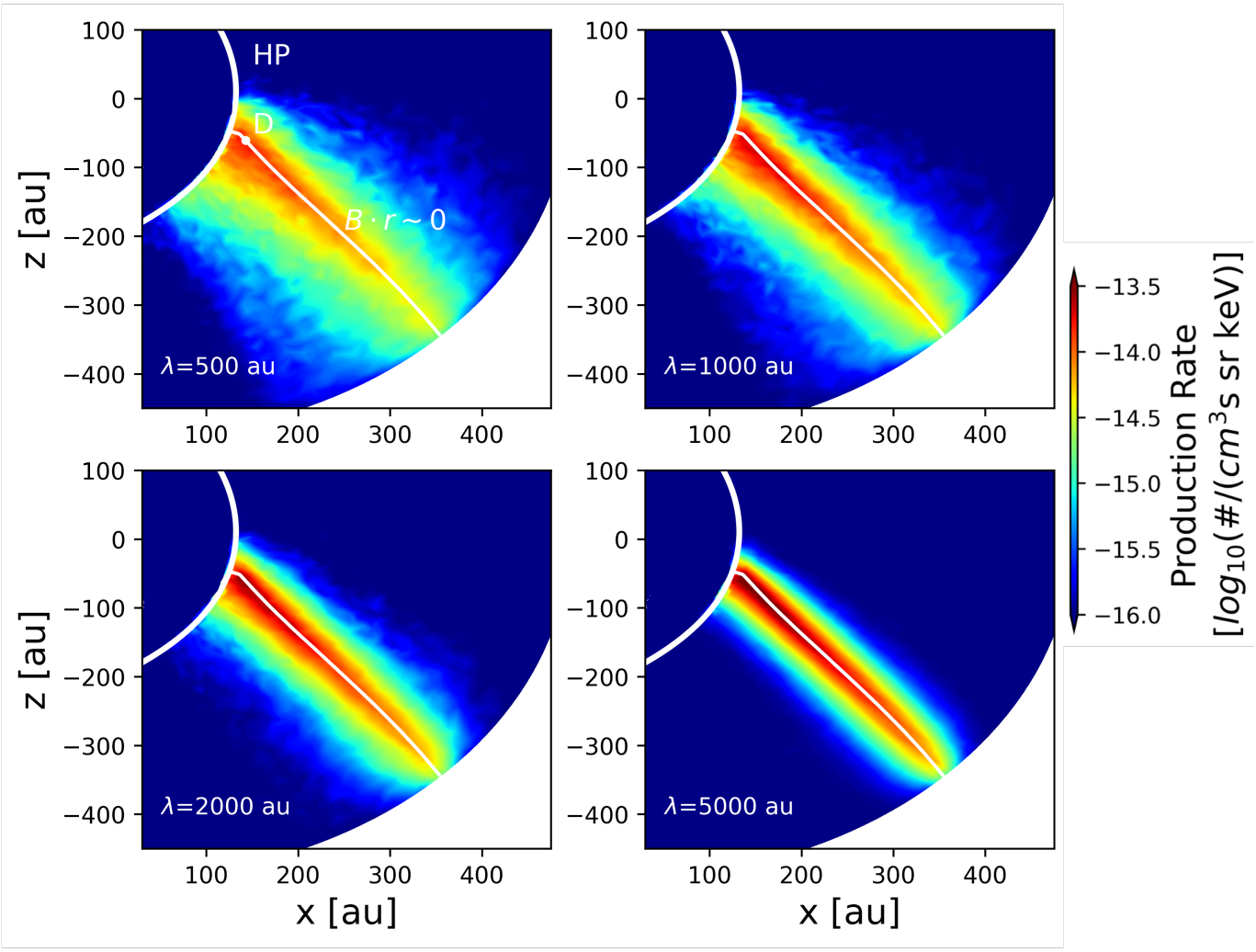

Figure 8. The spatial distribution of the ribbon ENA production rate for ESA 4 (1.74 keV) energy passband at meridian cut through the nose of the heliosphere in J2000 coordinate with parallel mean free paths $\lambda = 500$, 1000, 2000, and 5000 au, respectively. Note that the ENAs shown here are only those that can be detected at 1 au. The white thick curves represent the heliopause, and the thin white lines represent the surface where the ISMF is perpendicular to the LOS, i.e., $\boldsymbol{B} \bullet \boldsymbol{r} \sim 0$. The white dot, marked as "D," is the region in which we show the velocity distribution of PINS in Section 3.5.

which is consistent with the features shown in Figure 5. Additionally, at $\phi = 315°$, the $\lambda = 1000$ au case is the most comparable to observations.

Figure 7 also shows that the ENA intensity profiles of the simulated ribbon have a sharper slope at the outer edge and a more gradual slope at the inner edge. This asymmetry in the ribbon intensity profile is similar to that in the isotropic scattering case by E. J. Zirnstein et al. (2019). The asymmetry of the profile of the ENA intensity at the nose slice can be explained by the geometry of the $\boldsymbol{B} \bullet \boldsymbol{r} \sim 0$ surface caused by the draping of the ISMF around the HP. Since the source region of the ribbon is generally along the $\boldsymbol{B} \bullet \boldsymbol{r} \sim 0$ surface, it creates a ribbon profile asymmetry with a more gradual slope at the inner edge of the ribbon than at the outer edge. This asymmetry was also demonstrated by E. J. Zirnstein et al. (2018). The asymmetry becomes less obvious in the shorter λ case because the influence of the ISMF geometry becomes weaker with the wider ribbon source region due to stronger scattering (see Figure 8).

However, the ribbon-separated IBEX maps in Figure 7 do not show strong asymmetric ribbon profiles in any of the selected slices, likely because we used averaged NSW data over nearly a solar cycle. This averaging process may have smoothed out any short-term asymmetries. In fact, S. J. Noh et al. (2025) have shown detailed yearly ribbon-separated IBEX maps, revealing that the skewness of the ribbon can vary by year, energy, and azimuthal slice. We defer a detailed comparison between the time-dependent simulations and yearly IBEX maps to future work.

3.4. Spatial Distribution of Ribbon ENA Production Rate

To better understand how the spatial distribution of the ribbon ENAs is affected by the scattering of the PINS beyond the HP, Figure 8 shows the ribbon ENA production rate at a meridian cut through the nose of the heliosphere in ecliptic J2000 coordinates. Note that the ENAs shown here are only those that can be detected at 1 au. The thick white curves represent the heliopause, and the thin white curves represent the surface where the ISMF is perpendicular to the LOS, i.e., $\boldsymbol{B} \cdot \boldsymbol{r} \sim 0$.

As one can see, the strongest emissions in the ribbon source region are generally close to the HP and around the $\boldsymbol{B} \bullet \boldsymbol{r} \sim 0$ surface. The emissions become weaker at regions farther away from the HP as a result of the expansion of the NSW beyond

the HP. The ribbon source region does not extend radially from the Sun, but follows the $\boldsymbol{B}\cdot\boldsymbol{r}\sim 0$ surface (the thin white line), which is curved because of the draping of the ISMF around the heliopause, similar to the behavior shown in E. J. Zirnstein et al. (2016b, 2018). For this meridional cut (shown in the $\phi = 0^\circ$ panel of Figure 7), it results in a more gradual change in the ENA intensity to the north of the $\boldsymbol{B}\bullet\boldsymbol{r}\sim 0$ surface (inner edge of the ribbon) than to the south (outer edge of the ribbon).

Figure 8 shows that as the scattering becomes weaker (i.e., increasing λ), the source region of the ribbon ENA is more concentrated close to the $\boldsymbol{B}\bullet\boldsymbol{r}\sim 0$ surface, and the peak emission intensity becomes stronger. This feature suggests that weaker scattering leads to a more anisotropic pitch-angle distribution of PUIs in the ribbon ENA source region, reducing deviations from their original pitch angle (the angle between the radial direction and the magnetic field). Our results show that the weakly scattering scenario, represented with a large mean free path case, can produce simulated ENA intensities consistent with the observed IBEX ribbon. Conversely, strong PUI scattering results in a nearly isotropic pitch-angle distribution. This broadens the secondary ENA source region and suppresses the ribbon signature, which is consistent with the prediction by, e.g., V. Florinski et al. (2010) and A. Mousavi et al. (2022). The spatial retention scenario (N. A. Schwadron & D. J. McComas 2013) similarly assumes isotropy but gives enhanced PUI densities in the ribbon ENA source region. However, simulations based on this mechanism produce ribbon intensities far lower than observed (E. J. Zirnstein et al. 2019). Further details on the velocity distribution are provided in Section 3.5.

In Figure 8, we also see that the source region is not symmetric about the $\boldsymbol{B}\bullet\boldsymbol{r}\sim 0$ surface, but has a larger emission region to the south of the surface. This behavior is in part due to PUI advection with the southward flow of interstellar plasma around the HP. We confirmed the effects of advection by artificially turning off the advection term in the model and found that the southward shift of the source region is reduced. The other reason for the southward extension of the ENA emission region is likely that the angle between the LOS and the magnetic field direction is different north and south of the $\boldsymbol{B}\bullet\boldsymbol{r}\sim 0$ surface due to the way in which the ISMF drapes around the HP. The geometry of the draped magnetic field to the south of the $\boldsymbol{B}\bullet\boldsymbol{r}\sim 0$ surface causes the SENA emission region observable from IBEX to extend further south than to the north.

3.5. Velocity Distribution of the PUIs beyond the Heliopause

Figure 9 shows the velocity distribution of PUIs at the time when the particles are initialized ("initial" panel) and the steady state distributions in the cases of $\lambda = 500$ au, $\lambda = 1000$ au, $\lambda = 2000$ au, and $\lambda = 5000$ au, respectively, in the "D" region shown in Figure 8, which is chosen with radial distance 156 ± 3 au and direction $(255^\circ \pm 2^\circ, -23^\circ \pm 2^\circ)$ in ecliptic coordinates. We can see that in the "initial" panel, the pitch-angle cosine is about $\mu = 0$, confirming that the "D" region is on the $\boldsymbol{B}\bullet\boldsymbol{r}\sim 0$ plane. The pitch-angle distributions clearly show that the PINS is less scattered for a larger λ, which is consistent with the spatial distribution of the ribbon ENA production shown in Figure 8.

Our results show that the pitch-angle distributions need to be highly anisotropic in order to explain the IBEX ribbon in the weakly scattering scenario (D. J. McComas et al. 2009b; J. Heerikhuisen et al. 2010). Meanwhile, the PUI distribution can be strongly scattered, as shown by V. Florinski et al. (2010), A. Mousavi et al. (2022), and in the spatial retention model (N. A. Schwadron & D. J. McComas 2013; E. J. Zirnstein et al. 2019). As discussed earlier, the stability of the ring-beam-like distribution of PINS is still in debate, and our current work does not compare different mechanisms. Note that in our work, we simplify the physics in PUI scattering by assuming a prescribed mean free path, and some physics in the pitch-angle evolution might be neglected, e.g., microinstabilities of the ring-beam-like PINS distribution and turbulent mirroring. However, by comparing with the observations, our model could provide an "equivalent" mean free path in the PUI scattering, which can be used to study the transport of PUIs outside the heliopause and examine the PUI scattering mechanisms for the IBEX ribbon ENA production.

In Figure 9, the velocity distribution of PUIs has a larger intensity at $\mu > 0$ (corresponding to the direction toward the equatorial plane). This is probably because of the mixed influence of several factors, e.g., the geometry of the draped ISMF, PUI advection, and the distribution of initialized PUIs in the simulation. Given that this problem is beyond this paper, we leave it to a future study.

4. Summary

In this paper, we present a new global model of the IBEX ribbon based on the secondary ENA mechanism. Our model incorporates a realistic background plasma and magnetic field for the heliosphere and the LISM, following the global heliosphere model in E. J. Zirnstein et al. (2021b). It also incorporates an NSW profile and the NSW profile for input of the parent neutral population for the PUIs outside the heliopause based on the neutral SW source model introduced in P. Swaczyna et al. (2016) and E. J. Zirnstein et al. (2019). We simulate the dynamics of the PUIs by solving the gyrophase-averaged focused transport equations. Additionally, we use prespecified parallel mean free paths to calculate the pitch-angle diffusion coefficients according to quasi-linear theory. We compare our synthetic ribbon sky maps with the IBEX data and examine the effects of PUI scattering on the ribbon properties.

From the simulation results in this paper, we find that stronger PUI pitch-angle scattering leads to a wider ribbon structure with lower ENA intensity. Compared with the IBEX data, mainly for the ESA 4 energy passband, we estimate that the parallel mean free path for 1 keV PUIs outside the heliopause is on the order of several thousand au, for which the intensities and the profiles of the ribbon in our simulation are more consistent with the observations.

We calculated the ribbon centers for each energy passband for different mean free paths and found that in the weaker scattering cases, the ribbon centers are closer to the mean ribbon center. We also found a shift of the ribbon centers toward the southwest from the low-energy passband to the high-energy passband, which is consistent with the observations. Our simulation results indicate that the PUI transport in the ribbon modeling has an influence on the position of the ribbon center.

We plotted the cross-sectional profiles of the ENA intensity in azimuthal slices of the ribbon-centered frame for ESA 4. The results show that as scattering becomes stronger, the peak intensity is higher and the width is narrower. In the slices

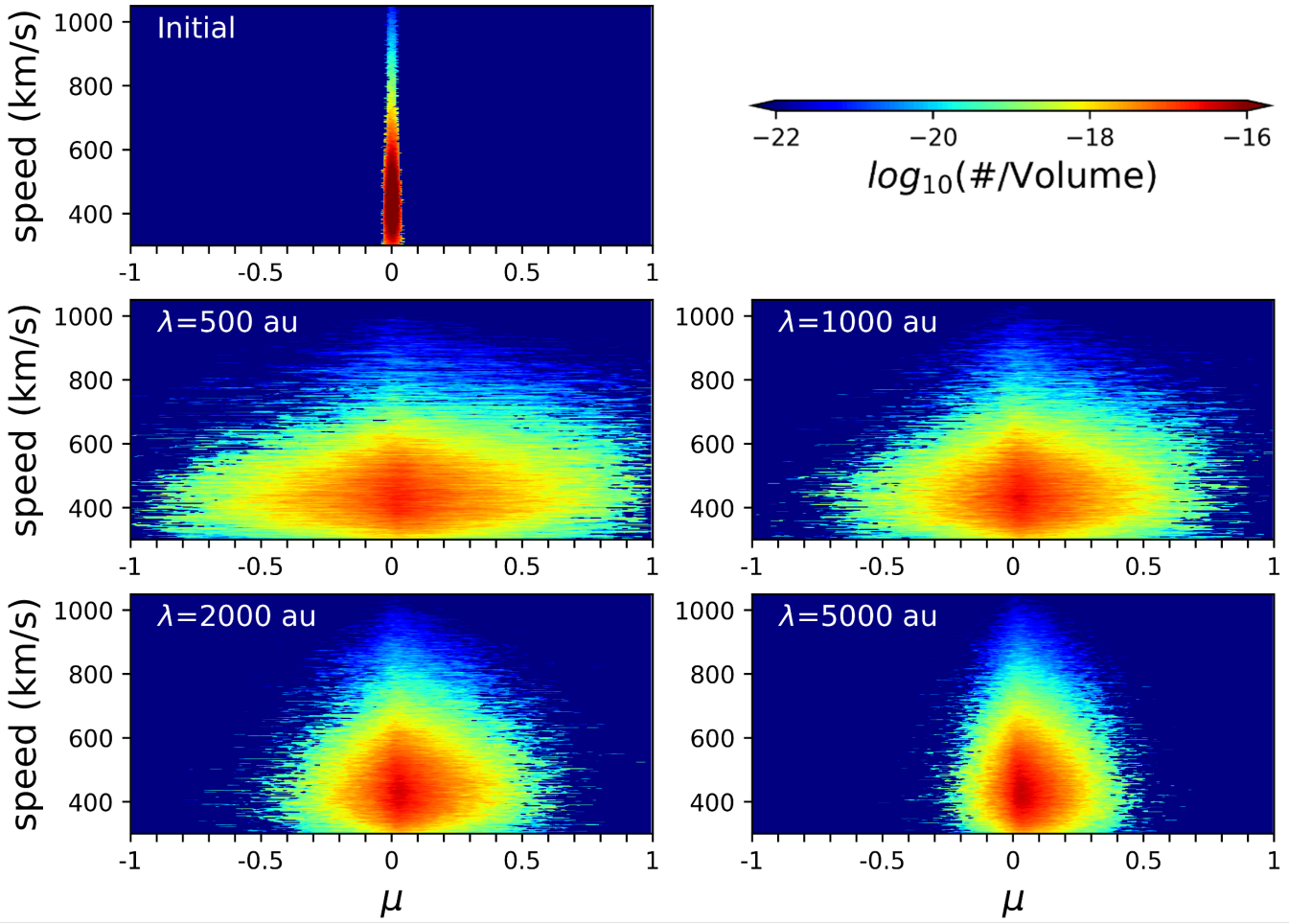

Figure 9. Velocity distribution of PUIs at the time when pseudoparticles are initialized ("initial" panel), and the steady state distributions in the cases of $\lambda = 500$ au, $\lambda = 1000$ au, $\lambda = 2000$ au, and $\lambda = 5000$ au, respectively, in the "D" region shown in Figure 8.

crossing the brightest emission regions (azimuthal angle $\phi = 45°$ and 270°), the case with a mean free path of 5000 au has a peak intensity and width that are most comparable to the observations. We also find that the profile slope at the inner edge of the ribbon is more gradual than at the outer edge, which can be explained by the ribbon source region bending away from the radial direction at a larger distance from the heliopause, along the surface where the magnetic field is perpendicular to the LOS, i.e., $\boldsymbol{B} \bullet \boldsymbol{r} \sim 0$. The ribbon source region shown in our simulation results becomes more concentrated around the $\boldsymbol{B} \bullet \boldsymbol{r} \sim 0$ surface as the mean free path increases, representing weaker scattering. Under this condition, the velocity distribution is more anisotropic, and this is needed to generate ENAs consistent with IBEX ribbon observations.

Our ribbon model, which includes a PUI transport module, has the ability to incorporate the PUI transport mechanism into global ribbon modeling and can potentially assist in determining which mechanism is more reasonable through comparison with observations.

Acknowledgments

This work at Los Alamos National Laboratory is supported by the Laboratory Directed Research and Development program under project No. 20220107DR.

ORCID iDs

Yifan Huang https://orcid.org/0000-0002-0422-2925
Fan Guo https://orcid.org/0000-0003-4315-3755
Eric J. Zirnstein https://orcid.org/0000-0001-7240-0618
Sung Jun Noh https://orcid.org/0000-0002-8032-7833
Hui Li https://orcid.org/0000-0003-3556-6568
Daniel B. Reisenfeld https://orcid.org/0000-0003-1874-9450
Jacob Heerikhuisen https://orcid.org/0000-0001-7867-3633

References

Beesley, L. J., Osthus, D., Moran, K. R., et al. 2023, arXiv:2302.03089
Berdichevsky, D. B. 2009, Voyager Mission, Detailed Processing of Weak Magnetic Fields; I—Constraints to the Uncertainties of the Calibrated Magnetic Field Signal in the Voyager Missions, NASA Goddard Space Flight Center, http://vgrmag.gsfc.nasa.gov/Berdichevsky-VOY_sensor_opu090518.pdf
Burlaga, L. F., Florinski, V., & Ness, N. F. 2018, ApJ, 854, 20
Chalov, S. V., Alexashov, D. B., McComas, D., et al. 2010, ApJL, 716, L99
Czechowski, A., & Grygorczuk, J. 2017, JPhCS, 900, 012004
Dayeh, M. A., McComas, D. J., Livadiotis, G., et al. 2011, ApJ, 734, 29
Dayeh, M. A., Zirnstein, E. J., Desai, M. I., et al. 2019, ApJ, 879, 84
Florinski, V., & Heerikhuisen, J. 2017, ApJ, 838, 50
Florinski, V., Heerikhuisen, J., Niemiec, J., & Ernst, A. 2016, ApJ, 826, 197
Florinski, V., Zank, G. P., Heerikhuisen, J., Hu, Q., & Khazanov, I. 2010, ApJ, 719, 1097
Fraternale, F., Pogorelov, N. V., & Bera, R. K. 2023, ApJ, 946, 97
Fraternale, F., Pogorelov, N. V., & Bera, R. K. 2024, ApJL, 974, L15
Funsten, H. O., Allegrini, F., Bochsler, P., et al. 2009a, SSRv, 146, 75

Funsten, H. O., Allegrini, F., Crew, G. B., et al. 2009b, Sci, 326, 964
Fuselier, S. A., Allegrini, F., Funsten, H. O., et al. 2009, Sci, 326, 962
Gamayunov, K., Zhang, M., & Rassoul, H. 2010, ApJ, 725, 2251
Gamayunov, K. V., Heerikhuisen, J., & Rassoul, H. 2017, ApJ, 845, 63
Gamayunov, K. V., Heerikhuisen, J., & Rassoul, H. K. 2019, ApJL, 876, L21
Giacalone, J., & Jokipii, J. R. 1999, ApJ, 520, 204
Giacalone, J., & Jokipii, J. R. 2015, ApJL, 812, L9
Giacalone, J., & Jokipii, J. R. 2020, ApJL, 897, L45
Heerikhuisen, J., Gamayunov, K. V., Zirnstein, E. J., & Pogorelov, N. V. 2016, ApJ, 831, 137
Heerikhuisen, J., Pogorelov, N. V., Zank, G. P., et al. 2010, ApJL, 708, L126
Heerikhuisen, J., Zirnstein, E., & Pogorelov, N. 2015, JGRA, 120, 1516
Heerikhuisen, J., Zirnstein, E. J., Funsten, H. O., Pogorelov, N. V., & Zank, G. P. 2014, ApJ, 784, 73
Isenberg, P. A. 1997, JGR, 102, 4719
Isenberg, P. A. 2014, ApJ, 787, 76
Isenberg, P. A. 2015, JPhCS, 577, 012014
Jokipii, J. R. 1966, ApJ, 146, 480
Kartavykh, Y. Y., Dröge, W., & Gedalin, M. 2016, ApJ, 820, 24
Kong, X., Chen, B., Guo, F., et al. 2022, ApJL, 941, L22
le Roux, J. A., & Webb, G. M. 2012, ApJ, 746, 104
Li, X., Guo, F., Chen, B., Shen, C., & Glesener, L. 2022, ApJ, 932, 92
Li, X., Guo, F., Li, H., & Li, S. 2018, ApJ, 866, 4
Lindsay, B. G., & Stebbings, R. F. 2005, JGRA, 110, A12213
McComas, D. J., Alimaganbetov, M., Beesley, L. J., et al. 2024, ApJS, 270, 17
McComas, D. J., Allegrini, F., Bochsler, P., et al. 2009a, SSRv, 146, 11
McComas, D. J., Allegrini, F., Bochsler, P., et al. 2009b, Sci, 326, 959
McComas, D. J., Bzowski, M., Dayeh, M. A., et al. 2020, ApJS, 248, 26
McComas, D. J., Bzowski, M., Frisch, P., et al. 2010, JGRA, 115, A09113
McComas, D. J., Bzowski, M., Fuselier, S. A., et al. 2015, ApJS, 220, 22
McComas, D. J., Lewis, W. S., & Schwadron, N. A. 2014, RvGeo, 52, 118
Min, K., & Liu, K. 2018, ApJ, 852, 39
Möbius, E., Liu, K., Funsten, H., Gary, S. P., & Winske, D. 2013, ApJ, 766, 129
Mousavi, A., Liu, K., & Min, K. 2020, ApJ, 901, 167
Mousavi, A., Liu, K., & Sadeghzadeh, S. 2022, ApJ, 940, 37
Noh, S. J., Reisenfeld, D. B., Beesley, L. J., et al. 2025, ApJ, 980, 8
Northrop, T. G. 1963, RvGSP, 1, 283
Osthus, D., Weaver, B. P., Beesley, L. J., et al. 2023, Technometrics, 66, 208
Pogorelov, N. V., Heerikhuisen, J., Mitchell, J. J., Cairns, I. H., & Zank, G. P. 2009, ApJL, 695, L31
Pogorelov, N. V., Zank, G. P., Borovikov, S. N., et al. 2008, in ASP Conf. Ser. 385, Numerical Modeling of Space Plasma Flows, ed. N. V. Pogorelov, E. Audit, & G. P. Zank (San Francisco, CA: ASP), 180
Qin, G., Zhang, M., Dwyer, J. R., & Rassoul, H. K. 2004, ApJ, 609, 1076
Qin, G., Zhang, M., Dwyer, J. R., Rassoul, H. K., & Mason, G. M. 2005, ApJ, 627, 562
Rankin, J. S., McComas, D. J., Zirnstein, E. J., Burlaga, L. F., & Heerikhuisen, J. 2023, ApJL, 945, L31
Reisenfeld, D. B., Bzowski, M., Funsten, H. O., et al. 2021, ApJS, 254, 40
Roelof, E. C. 1969, in Lectures in High-Energy Astrophysics, ed. H. Ögelman & J. R. Wayland (Washington, DC: NASA), 111
Ruffolo, D. 1995, ApJ, 442, 861
Schwadron, N. A., Bzowski, M., Crew, G. B., et al. 2009, Sci, 326, 966
Schwadron, N. A., & McComas, D. J. 2013, ApJ, 764, 92
Schwadron, N. A., & McComas, D. J. 2019, ApJ, 887, 247
Skilling, J. 1975, MNRAS, 172, 557
Sokół, J. M., Bzowski, M., Kubiak, M. A., et al. 2015b, ApJS, 220, 29
Sokół, J. M., Swaczyna, P., Bzowski, M., & Tokumaru, M. 2015a, SoPh, 290, 2589
Summerlin, E. J., Viñas, A. F., Moore, T. E., Christian, E. R., & Cooper, J. F. 2014, ApJ, 793, 93
Swaczyna, P., Bzowski, M., & Sokół, J. M. 2016, ApJ, 827, 71
Swaczyna, P., McComas, D. J., Zirnstein, E. J., et al. 2020, ApJ, 903, 48
Wang, Y., Qin, G., & Zhang, M. 2012, ApJ, 752, 37
Webb, G. M. 1985, ApJ, 296, 319
Wijsen, N., Aran, A., Pomoell, J., & Poedts, S. 2019, A&A, 622, A28
Xu, S., & Li, H. 2023, ApJ, 957, 97
Zhang, M. 1999, ApJ, 513, 409
Zhang, M. 2006, JGRA, 111, A04208
Zhang, M., Qin, G., & Rassoul, H. 2009, ApJ, 692, 109
Zhang, M., & Zhao, L. 2017, ApJ, 846, 107
Zirnstein, E. J., Dayeh, M. A., & Heerikhuisen, J. 2021a, ApJ, 908, 35
Zirnstein, E. J., Dayeh, M. A., Heerikhuisen, J., McComas, D. J., & Swaczyna, P. 2021b, ApJS, 252, 26
Zirnstein, E. J., Funsten, H. O., Heerikhuisen, J., & McComas, D. J. 2016a, A&A, 586, A31
Zirnstein, E. J., Giacalone, J., Kumar, R., et al. 2020, ApJ, 888, 29
Zirnstein, E. J., Heerikhuisen, J., & Dayeh, M. A. 2018, ApJ, 855, 30
Zirnstein, E. J., Heerikhuisen, J., Funsten, H. O., et al. 2016b, ApJL, 818, L18
Zirnstein, E. J., Heerikhuisen, J., & McComas, D. J. 2015, ApJL, 804, L22
Zirnstein, E. J., Heerikhuisen, J., McComas, D. J., & Schwadron, N. A. 2013, ApJ, 778, 112
Zirnstein, E. J., McComas, D. J., Schwadron, N. A., et al. 2019, ApJ, 876, 92
Zirnstein, E. J., Swaczyna, P., Dayeh, M. A., & Heerikhuisen, J. 2023, ApJ, 949, 45
Zuo, P., Zhang, M., Gamayunov, K., Rassoul, H., & Luo, X. 2011, ApJ, 738, 168